NASA/TM-20250008763



Conceptual Design Studies of Zero-Emission Electric Aircraft Powered by a Strayton Combined Cycle Propulsion System

Marie Vaucher
University of Michigan, Ann Arbor, Michigan

Cody Karcher
Sandia National Laboratories, Albuquerque, New Mexico

Greeta Thaikattil and Rodger Dyson
Glenn Research Center, Cleveland, Ohio

Joaquim R. R. A. Martins
University of Michigan, Ann Arbor, Michigan

November 2025

NASA STI Program Report Series

Since its founding, NASA has been dedicated to the advancement of aeronautics and space science. The NASA scientific and technical information (STI) program plays a key part in helping NASA maintain this important role.

The NASA STI program operates under the auspices of the Agency Chief Information Officer. It collects, organizes, provides for archiving, and disseminates NASA's STI. The NASA STI program provides access to the NTRS Registered and its public interface, the NASA Technical Reports Server, thus providing one of the largest collections of aeronautical and space science STI in the world. Results are published in both non-NASA channels and by NASA in the NASA STI Report Series, which includes the following report types:

- TECHNICAL PUBLICATION.
  Reports of completed research or a major significant phase of research that present the results of NASA programs and include extensive data or theoretical analysis. Includes compilations of significant scientific and technical data and information deemed to be of continuing reference value. NASA counterpart of peer-reviewed formal professional papers but has less stringent limitations on manuscript length and extent of graphic presentations.

- TECHNICAL MEMORANDUM.
  Scientific and technical findings that are preliminary or of specialized interest, e.g., quick release reports, working papers, and bibliographies that contain minimal annotation. Does not contain extensive analysis.

- CONTRACTOR REPORT.
  Scientific and technical findings by NASA-sponsored contractors and grantees.

- CONFERENCE PUBLICATION.
  Collected papers from scientific and technical conferences, symposia, seminars, or other meetings sponsored or cosponsored by NASA.

- SPECIAL PUBLICATION.
  Scientific, technical, or historical information from NASA programs, projects, and missions, often concerned with subjects having substantial public interest.

- TECHNICAL TRANSLATION.
  English-language translations of foreign scientific and technical material pertinent to NASA's mission.

Specialized services also include organizing and publishing research results, distributing specialized research announcements and feeds, providing information desk and personal search support, and enabling data exchange services.

For more information about the NASA STI program, see the following:

- Access the NASA STI program home page at http://www.sti.nasa.gov

NASA/TM-20250008763



Conceptual Design Studies of Zero-Emission Electric Aircraft Powered by a Strayton Combined Cycle Propulsion System

Marie Vaucher
University of Michigan, Ann Arbor, Michigan

Cody Karcher
Sandia National Laboratories, Albuquerque, New Mexico

Greeta Thaikattil and Rodger Dyson
Glenn Research Center, Cleveland, Ohio

Joaquim R. R. A. Martins
University of Michigan, Ann Arbor, Michigan

National Aeronautics and
Space Administration

Glenn Research Center
Cleveland, Ohio 44135

November 2025

Acknowledgments

The authors would like to thank Eytan Adler for his guidance, support, and general expertise in hydrogen aircraft modeling, and Venkat Subramaniam for his work in aircraft weight modeling that was integrated into OpenConcept.
Funding for this research was provided by NASA under grant number NNX11AI19A.

This report contains preliminary findings, subject to revision as analysis proceeds.

This work was sponsored by the Advanced Air Vehicles Program at the NASA Glenn Research Center.

Trade names and trademarks are used in this report for identification only. Their usage does not constitute an official endorsement, either expressed or implied, by the National Aeronautics and Space Administration.

Level of Review: This material has been technically reviewed by technical management.

This report is available in electronic form at https://www.sti.nasa.gov/ and https://ntrs.nasa.gov/

NASA STI Program/Mail Stop 050
NASA Langley Research Center
Hampton, VA 23681-2199

Abstract

Electric propulsion is a defining feature of many of the future concepts currently being studied for sustainable aviation, but power generation for this type of propulsion architecture remains an open research question. Electric batteries and hydrogen fuel cells are both being studied in current literature, but these options remain at a low TRL and lack a clear path to a feasible design for missions that currently make up the majority of the air transportation network. This work considers a combined Stirling-Brayton (ie Strayton) hybrid cycle power generator composed primarily of existing technologies, and evaluates its performance on an ATR-72 (regional turboprop transport) type aircraft. Performance comparisons reveal that the Strayton powered aircraft burns 50% less fuel than the turboprop baseline and 30% less than a notional hydrogen powered fuel cell. Given these results, we conclude that the Strayton engine is a highly promising option for future propulsion architectures, particularly as a transition technology and but also as a potential long-term replacement for existing turbo-machines.

Contents

List of Figures **3**

List of Tables **4**

1 Flight Performance Modeling **5**
1.1 List of symbols . . . 5
1.2 Measuring Aircraft Performance . . . 5
1.3 Aircraft Performance Overview . . . 5
1.4 Performance Modeling Approach . . . 6
1.5 Mission Simulation . . . 6
1.6 OpenConcept . . . 7

2 Aircraft Modeling **9**
2.1 List of Symbols . . . 9
2.2 ATR72–600 . . . 9
2.3 B737–800 . . . 12

3 Powertrain Modeling **14**
3.1 Turboprop . . . 14
3.2 Turbofan . . . 16
3.3 Hydrogen Fuel Cells . . . 17
3.4 Strayton Power Generator . . . 29

4 Case Study: ATR72–600 **33**
4.1 Strayton Kerosene . . . 33
4.2 Hydrogen Turboprop Retrofit . . . 33
4.3 Strayton Retrofit . . . 35
4.4 Fuel Cells Retrofit . . . 37
4.5 Global Comparison . . . 38

5 Case Study: B737–800 **40**
5.1 Strayton Kerosene Retrofit . . . 40

6 Conclusions and Future Work **41**
6.1 Conclusions and Recommendations . . . 41
6.2 Integration with the TREES System . . . 41
6.3 Clean Sheet Design Studies . . . 41
6.4 Higher Fidelity Models . . . 42

References **43**

List of Figures

1 Openconcept mission 6
2 ATR72–600 10
3 TOW Kerosene model 11
4 B737–800 12
5 TOW Kerosene model 14
6 A simple fuel cell 18
7 The breakdown of a fuel cell voltage (efficiency) curve (taken from [1]) 22
8 A typical fuel cell power curve (taken from [1]) 23
9 Variation of pressure for both SOFCs and PEMFCs 27
10 Study of SOFCs with varying temperature 27
11 Study of PEMFCs with varying temperature 28
12 Trade-off between fuel cell size and efficiency, large fuel cells are towards the left of the chart, smaller fuel cells towards the right 28
13 A T-s Diagram representing the Brayton Cycle 29
14 A T-s Diagram representing the Brayton Cycle 30
15 Comparison between the Strayton model from [2] and the OpenMDAO model created for the aircraft design case studies 32
16 TOW mass breakdown for Kerosene Strayton model 34
17 ATR72–600 hydrogen tanks 35
18 TOW Hydrogen model 36
19 TOW Hydrogen Strayton model 37
20 TOW fuel cells model 38
21 TOW Strayton Kerosene model 41

List of Tables

1 ATR72–600 range for each flight segment . . . 7
2 B737–800 range for each flight segments . . . 7
3 ATR72–600 flight data . . . 7
4 B737–800 flight data . . . 7
5 Type of propulsion for ATR72–600 . . . 9
6 ATR72–600 airframe data . . . 10
7 ATR72–600 Aerodynamic data . . . 10
8 ATR72–600 weight data . . . 11
9 Type of propulsion for B737–800 . . . 12
10 B737–800 airframe data . . . 12
11 B737–800 Aerodynamic data . . . 13
12 B737–800 weight data . . . 13
13 ATR72–600 propulsion weight data . . . 15
14 ATR72–600 propulsion data . . . 15
15 B737–800 propulsion weight data . . . 17
16 B737–800 propulsion data . . . 17
17 Constants for the diffusivity model when using pairs of gases (eg: H_2, O_2, N_2) . . . 19
18 Constants for the diffusivity model when using a nonpolar gas (eg: H_2, O_2, N_2) and water (H_2O) . . . 20
19 Parameters for the diffusivity model . . . 20
20 Parameters for computing the thermodynamic efficiency of fuel cells . . . 20
21 Parameters for SOFC modeling . . . 25
22 Parameters for PEMFC modeling . . . 25
23 Parameters for the Strayton model . . . 32
24 ATR72–600 Strayton-kerosene propulsion weight data . . . 33
25 ATR72–600 Strayton-kerosene propulsion data . . . 33
26 Strayton retrofit performances . . . 34
27 ATR72–600 Strayton-hydrogen propulsion weight data . . . 35
28 ATR72–600 Strayton-hydrogen propulsion data . . . 35
29 Strayton hydrogen retrofit performance . . . 36
30 ATR72–600 fuel cells propulsion weight data . . . 37
31 ATR72–600 fuel cells propulsion data . . . 38
32 Fuel cells retrofit performance . . . 38
33 Fuel per passenger-mile (lbs/nmi) . . . 39
34 B737–800 Strayton-kerosene propulsion weight data . . . 40
35 B737–800 Strayton-kerosene propulsion data . . . 40
36 Strayton kerosene retrofit performances . . . 40

1 Flight Performance Modeling

1.1 List of symbols

D	Drag
$\dot{f}$	Fuel flow
g	Gravitational constant
L	Lift
R	Range of flight
SFC	Specific fuel consumption
T	Thrust
V	Speed
W	Weight

1.2 Measuring Aircraft Performance

In the context of net zero emissions policy, the goal of the present study is to evaluate the performance of various promising propulsion technologies thanks to different metrics:

- MTOW
- Fuel consumed
- Emissions

Obtaining these metrics requires aircraft numerical models and a computational architecture: OpenConcept.

1.3 Aircraft Performance Overview

In this work, we consider different models of powertrain systems. The performance of these powertrains will be evaluated through the lens of their performance on an aircraft system, which can be analyzed using the Breguet range equation. To fit with the purpose of evaluating the fuel consumption of various propulsion technologies, the equation is modified to appears as a fuel weight calculation.

$$R = \frac{1}{g}\frac{V}{SFC}\frac{L}{D}\ln\left(\frac{W_{\text{initial}}}{W_{\text{final}}}\right) \tag{1.1}$$

$$W_{\text{fuel}} = \left(\exp\left(\frac{gR\dot{f}}{TV(L/D)}\right) - 1\right)(W_{\text{airframe}} + W_{\text{powertrain}} + W_{\text{payload}}) \tag{1.2}$$

Many of these quantities of interest are relevant to the aircraft model. These findings are presented in a future section along with their influence on the overall performance.
As is typical, weight has a strong negative impact on fuel consumption, and powertrain systems must be kept as light as possible.

1.4 Performance Modeling Approach

To analyze the performance of the aircraft and integrated propulsion system, this work implements a two dimensional model of the aircraft flight dynamics to predict fuel burn for some given mission. This model represents a higher fidelity alternative to the Breguet range equation and allows for the consideration of numerous types of flight segments including takeoff, climb, cruise, and descent.

The aircraft is required to maintain equilibrium throughout all flight phases, ie, the aircraft is always assumed to be in steady flight with the exception of takeoff and landing segments. Although this approximation may seem highly imprecise, the various simulations carried out on missions with known performances enable us to validate it.

During the mission, the forces applied to the aircraft are evaluated from the model, taking into account flight and atmospheric conditions. In order to maintain the aircraft in a state of equilibrium, the throttle to be applied is determined so that the sum of the forces is equal to zero.

1.5 Mission Simulation

In this study, complete missions are simulated in order to evaluate the performance of the aircraft models developed over the entire duration of a flight. Each mission consists of three phases: the main mission, the reserve mission and a holding phase. The first two phases are divided into three segments: climb, cruise, descent.

Aircraft dynamics modeling takes into account the flight parameters for each phase, in particular climb rate, speed and cruise altitude. These parameters enable us to calculate the atmospheric conditions for each node, and thus determine the aircraft's attitude with greater precision.

Flight data for the two commercial models studied are retrieved from the FlightRadar application, which records flight data from all flights made. These data are presented in Table 3 and Table 4. For the sake of consistency between the various simulations, the data presented are valid whatever the technology studied.

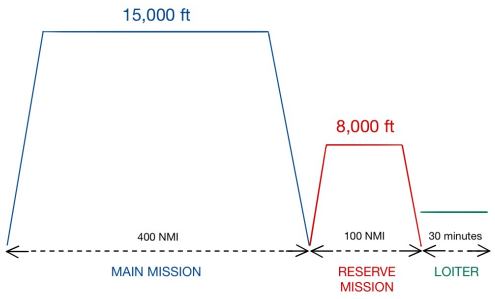


Figure 1: Openconcept mission

Table 1: ATR72–600 range for each flight segment

	Main Mission	Reserve Mission
Range	400 nmi	100 nmi

	Main mission	Reserve mission
Range	2800nmi	100nmi

Table 2: B737–800 range for each flight segments

		Vertical speed	Equivalent air speed	Altitude
Main mission	Climb	1500 ft/min	140 kn	0 ft–15 000 ft
Main mission	Cruise	0 ft/min	250 kn	15 000 ft
Main mission	Descent	-700 ft/min	190 kn	15 000 ft–0 ft
Reserve mission	Climb	1800 ft/min	150 kn	0 ft–8 000 ft
Reserve mission	Cruise	0 ft/min	250 kn	8 000 ft
Reserve mission	Descent	-500 ft/min	190 kn	8 000 ft–0 ft
Loiter		0 ft/min	240 kn	1 500 ft

Table 3: ATR72–600 flight data

		Vertical speed	Equivalent air speed	Altitude
Main mission	Climb	2300–400 ft/min	230–252 kn	0 ft–35 000 ft
Main mission	Cruise	0 ft/min	252 kn	35 000 ft
Main mission	Descent	-1300 ft/min– -800 ft/min	252 kn–250 kn	35 000 ft–0 ft
Reserve mission	Climb	3000–2300 ft/min	230 kn	0 ft–15 000 ft
Reserve mission	Cruise	0 ft/min	250 kn	15 000 ft
Reserve mission	Descent	-800 ft/min	250 kn	15 000 ft–0 ft
Loiter		0 ft/min	250 kn	2 800 ft

Table 4: B737–800 flight data

1.6 OpenConcept

This work leverages OpenConcept [3], a tool package built on OpenMDAO [4]. It is a conceptual-level capability for aircraft design that includes gradient information. Initially developed for thermal management system design, OpenConcept has been used in a variety of applications: aircraft performance analysis, propulsion conceptual design, etc.

The tool requires an aircraft numerical model which provides drag, thrust and weight considering the flight parameters and atmospheric conditions. With this model, the tool has the capability to compute fuel consumption over time. This quantity of interest can then be used to quantify aircraft performance.

To provide drag, thrust and weight the user is free to take its own numerical models. However a big advantage of OpenConcept is to store basic components in different categories: thermal, propulsion,

weight, aerodynamics. These individual components have been previously validated with manufacturers data. OpenConcept on its own can produce a full aircraft model with no additional models.

2 Aircraft Modeling

In this study, we will be looking at the performance of two types of aircraft: an ATR72-600 regional turboprop and a B737–800 medium-haul aircraft. The aim of the study is to compare the performance of the Strayton engine with propulsion technologies that are considered promising: in particular, hydrogen propulsion in diverse context. The models used have already been developed by the team over the past few months for hydrogen propulsion studies.

2.1 List of Symbols

AR	Aspect ratio
C_L	Lift coefficient
CD_0	Zero-lift drag coefficient
e	Oswald efficiency
q	Dynamic pressure
S_{ref}	Aircraft reference area (wing planform area)

2.2 ATR72–600

The ATR72-600 is a single-aisle regional transport aircraft equipped with two turboprops. There are multiple reasons for this aircraft to fit our study. First, the use of hydrogen as a fuel implies the presence of liquid hydrogen tanks. The imposing structure and high mass of these tanks means that they have to be moved from place in the aircraft, no longer in the wings but at the rear. Their presence therefore means having to eliminate rows of passengers. This loss of passengers is even more significant, and therefore disadvantageous for long-haul flights. It is this trend that is driving the study of regional aircraft for hydrogen propulsion. Then, Universal Hydrogen has already developed a demonstrator of an ATR72–600, which made its maiden flight in April 2023. It therefore seemed appropriate to test the performance of the Strayton engine on this model of aircraft, hence the choice of the ATR72–600. Five different types of propulsion will be studied for this model, grouped into two categories: kerosene propulsion and hydrogen propulsion. They are detailed in the Table 5.

Table 5: Type of propulsion for ATR72–600

	Kerosene propulsion	Hydrogen propulsion
Turboprop	x	x
Strayton	x	x
Fuel cells		x

2.2.1 Geometry

Figure 2 presents the model of ATR72–600.
The Table 6 shows the model's main airframe data.

2.2.2 Aerodynamics

The drag is divided in two categories: parasitic drag and induced drag. Zero-lift drag coefficient buildup for transport aircraft is based on a combination of methods from Roskam, Raymer, and the approach presented by OpenVSP [5] based on the computation of form factors and skin friction



Figure 2: ATR72–600

Table 6: ATR72–600 airframe data

Category	Quantity	Value	Units
Wing	Sref	61	m**2
	AR	12	
	Wingspan	27	m
	c4sweep	0	deg
Fuselage	Width	3.5	m
	Length	27.2	m
	Height	2.6	m

coefficient for fuselage, horizontal stabilizer, vertical stabilizer, and wing. An additional drag coefficient is taken into account in take-off configuration with flaps and landing gear. The induced drag is calculated based on a polar drag formulation:

$$\text{Drag} = qS_{ref}\left(CD_0 + \frac{C_L^2}{\pi eAR}\right) \tag{2.1}$$

The Table 7 shows the model's main aerodynamic data obtained with these models.

Table 7: ATR72–600 Aerodynamic data

Quantity	Value
Oswald efficiency	0.85
Zero lift drag coefficient (takeoff)	0.025
Zero lift drag coefficient (cruise)	0.024
Maximum lift coefficient (takeoff)	1.7

2.2.3 Weights

The weight of the aircraft model is calculated in two steps. The first step is out-of-mission OEW calculation. This weight model is built with equations provided by Roskam and Raymer, based on the geometric, propulsion, and payload parameters supplied by the manufacturer.

The Table 8 shows the consistency of the weight quantities calculated compared to those provided by the manufacturer. The relative error is sufficiently small to validate the model.

Table 8: ATR72–600 weight data

	Numerical model	Manufacturer	Relative error (%)
OEW (kg)	13603	13600	0.02
MTOW (kg)	22687	23000	1.36
Block fuel (kg)	1113	1115	0.18

Next step is to compute take-off weight. All missions will be flown at maximum payload capacity of 7400 kg. The block fuel indicated is for the maximum range flight of 740 nmi, with a 100 nmi reserve and 30 minutes loiter. These quantities added to OEW constitute the TOW. The Figure 3 presents the TOW mass breakdown.

The aircraft model integrates the fuel flow over time and subtracts the mass calculated to the TOW to obtain the aircraft weight for each node.

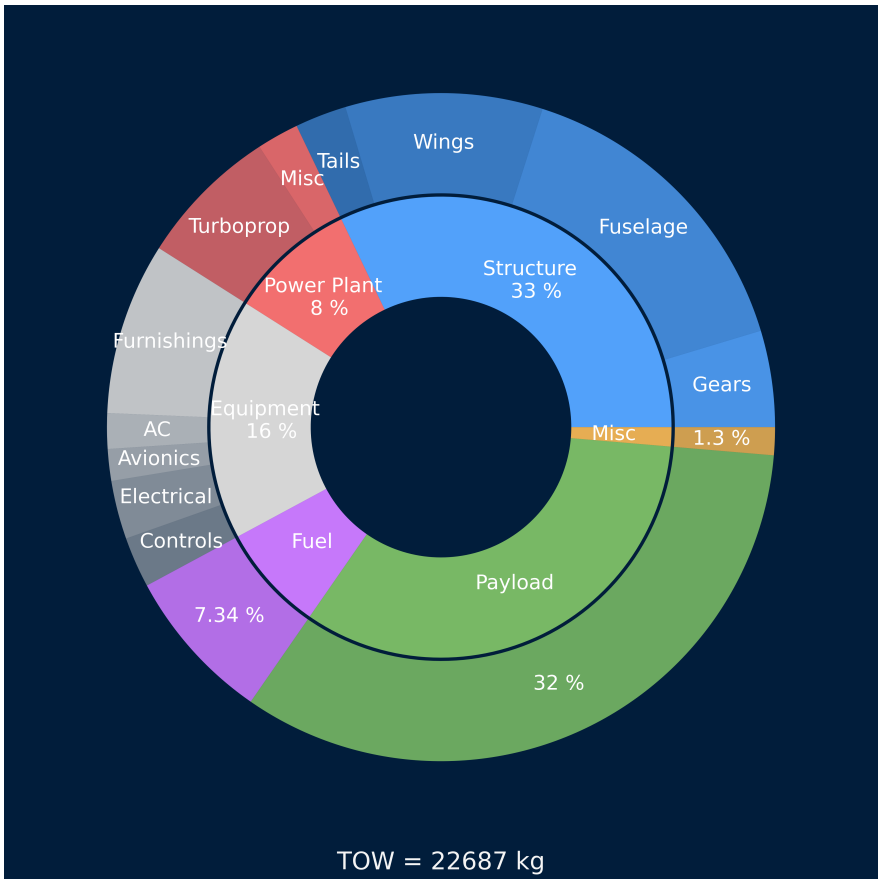


Figure 3: TOW Kerosene model

2.3 B737–800

The B737–800 is a single aisle turbofan aircraft fitted for medium-range flights. This performance study on this aircraft will enable us to extend our work to a broader context. However, for a flight of this distance, the quantities of fuel are greater, and therefore the hydrogen tanks larger, to the point where too many passenger rows have to be eliminated. Such a retrofit would not make a commercial flight profitable. For this reason, we are not studying a hydrogen-powered retrofit for this model. The two propulsion models chosen for the B737–800 are listed in Table 9. In a future study, we can carry out a clean-sheet optimization for this model and introduce a competitive hydrogen propulsion system.

Table 9: Type of propulsion for B737–800

	Kerosene propulsion
Turboprop	x
Strayton	x

2.3.1 Geometry

Figure 4 presents the model of ATR72–600.



Figure 4: B737–800

The Table 10 shows the model's main airframe data.

Table 10: B737–800 airframe data

Category	Quantity	Value	Units
Wing	Sref	124.6	m**2
	AR	9.45	
	Wingspan	34	m
	c4sweep	25	deg
Fuselage	Width	4.01	m
	Length	38.08	m
	Height	3.76	m

2.3.2 Aerodynamics

The Table 11 shows the model's main aerodynamic data.

Table 11: B737–800 Aerodynamic data

Quantity	Value
Oswald efficiency	0.801
Zero lift drag coefficient (takeoff)	0.03
Zero lift drag coefficient (cruise)	0.01925
Maximum lift coefficient (takeoff)	2.16

2.3.3 Weights

The Table 12 shows the model's main weight data. The weight model is built with models provided by Roskam and Raymer, based on the geometric parameters supplied by the manufacturer. The block fuel indicated is for the maximum range flight of 2800 nmi, with a 100 nmi reserve and 30 minutes loiter.

Table 12: B737–800 weight data

	Numerical model	Manufacturer	Relative error (%)
OEW (kg)	41748.9	41413	0.81
MTOW (kg)	78348.5	79016	0.84
Block fuel (kg)	18599.5	18996	2.09

The Figure 3 presents the TOW mass breakdown. Payload is chosen has max payload and the block fuel is for the maximum range mission.

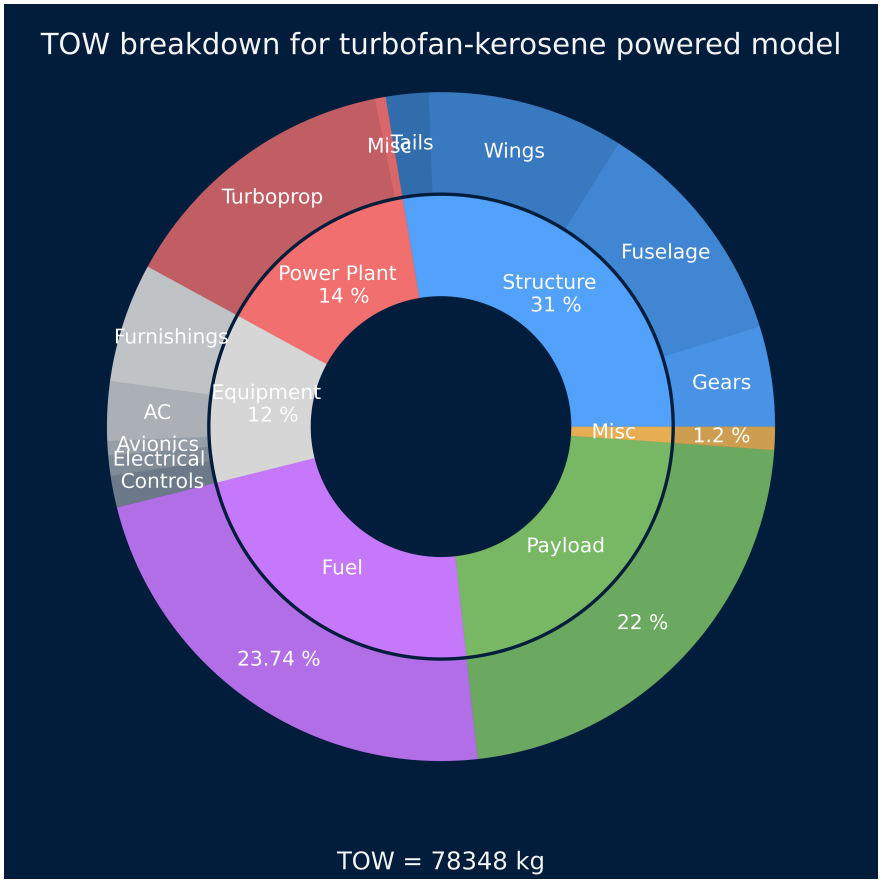


Figure 5: TOW Kerosene model

3 Powertrain Modeling

3.1 Turboprop

The propulsion system is composed of twin turboprops. The turboprop model is built with a turboshaft and a simple propeller model.

The complete turboprop model is designed to obtain the thrust generated by the turboprop from the throttle value proposed by the optimizer. To model the propulsion system of the ATR 72–600, we use conceptual models already contained in the OpenConcept library. A single turboprop model consists of two sub-elements: the turboshaft and a propeller. Both models are based on the theory provided by Raymer [6].

The turboshaft model uses the throttle value to obtain the mechanical power developed by the engine, using the shaft power rating as a variable design. It assumes constant power specific fuel consumption and provides the necessary fuel flow considering the throttle. The optimizer sets a value for the shaft power rating to ensure that sufficient thrust is delivered for all phases of flight. Once this value has been set, the component calculates the engine weight from the power-to-weight ratio.

Secondly, the propeller model calculates the thrust generated from the mechanical work it receives. The model is representative of a constant-speed prop. A general, empirical efficiency map for a

constant speed turboprop is used for most of the flight regime. A static thrust coefficient map – from Raymer [6] – is used for advance ratio smaller than 0.2, at low speed. Linear interpolation from static thrust to dynamic thrust tables at J = 0.1 to J = 0.2. This model takes into account the diameter and number of propeller blades. Two options are available: 3 or 4 blades, and therefore do not correspond to our case of 6 blades. We are aware of this inaccuracy in the model, but feel that it has only a minor impact on the calculated performance, so we have decided to retain the 4-blades option. This component also calculates the mass of the propeller from its diameter, the number of blades and the engine power rating previously determined.

This model is integrated into the aircraft model by connecting to various variables that have a major impact on performance during flight:

- The fuel flow: the value of fuel flow is integrated as a function of time during the simulated mission to determine the mass of fuel consumed at each node. This weight is then subtracted from the take-off weight to obtain the aircraft weight at each node.
- The OEW: engine and propeller weights are added to the OEW.

To summarize, we listed the inputs, outputs and options below. The inputs to the model are:

- Shaft power rating: Rated power of the turboshaft
- Throttle: engine throttle which controls power and fuel flow. Produces 100% of rated power at throttle = 1. Should be in range 0 to 1 or slightly above 1.

The outputs to the model are:

- Shaft power out: Shaft power produced by the engine.
- Fuel flow consumed.
- Weight of the component.

The model has two options:

- Power specific fuel consumption.
- Weight per unit rated power.

Table 14 and Table 13show the model's main propulsion data.

Table 13: ATR72–600 propulsion weight data

	Turboshafts (2)	Fans (2)	Misc	Total
Mass (kg)	1098	424	424	1946

Table 14: ATR72–600 propulsion data

	Turboshaft	Fan	Total
Power (MW)	2.05	1.64	
Efficiency	0.30	0.8	0.24
Power-to-weight ratio (kW/kg)	3.7		

Converting a kerosene turboprop into a hydrogen turboprop involves a number of mechanical modifications that we won't go into here. These changes are not taken into account in our modeling, and we make the approximation that the engines remain the same in terms of mass and operation. The use of hydrogen as fuel changes the specific energy of the fuel, which will scale the fuel flow to deliver the same amount of energy to the engine. It doesn't change the fuel specific consumption engine value.

3.2 Turbofan

The OpenConcept turbofan model is an optimized N+3 GTF engine deck which can optionally be switched to CFM56. It is generated as a surrogate of pyCycle data. This version adds the rated thrust input which adds a multiplier on thrust and fuel flow to enable continuous scaling of the engine power.

This version of the engine can also be converted to hydrogen with the hydrogen option. It will scale the fuel flow by the ratio of LHV between jet fuel and hydrogen to deliver the same energy to the engine. This maintains the same thrust-specific energy consumption.
The CFM56 and N3 engine models only include data Mach 0.2 to 0.8 and up to 35,000 ft. Outside that range, the model is unreliable.
The inputs of this model are:

- Engine throttle: Controls power and fuel flow. Produces 100% of rated power at throttle = 1. Should be in range 0 to 1 or slightly above 1.
- Altitude.
- Mach number.
- Engine rating: desired thrust rating (sea level static) of each engine; the CFM56 thrust and fuel flow are scaled by this value divided by 27,300, while the N+3 thrust and fuel flow are scaled by this value divided by 28,620.

The outputs of the model are:

- Thrust: Thrust developed by the engine.
- Fuel flow: Fuel flow consumed.
- Surge margin or T4: Surge margin if engine is "N3" or T4 if engine is "CFM56".

The model has also two options, depending on the propulsion system studied:

- Hydrogen: True to convert fuel flow to an equivalent fuel flow of hydrogen by multiplying by the ratio of lower heating value between jet fuel and hydrogen. Otherwise it will keep the fuel flow from the jet fuel-powered version of the engine deck.
- Engine deck to use, valid options are "N3" and "CFM56", by default "N3"

This model is integrated into the aircraft model by connecting to various variables that have a major impact on performance during flight:

- The fuel flow: the value of fuel flow is integrated as a function of time during the simulated mission to determine the mass of fuel consumed at each node. This weight is then subtracted from the take-off weight to obtain the aircraft weight at each node.

- The OEW: turbofan weight is added to the OEW.

Table 15 and Table 16 show the model's main propulsion data.

Table 15: B737–800 propulsion weight data

	Turbofans (2)	Misc	Total
Mass (kg)	2225	1143	5593

Table 16: B737–800 propulsion data

	Turbofan
Power (MW)	
Efficiency	0.35
Power-to-weight ratio (kW/kg)	6

3.3 Hydrogen Fuel Cells

3.3.1 Background

The purpose of the aircraft propulsion system is to convert energy stored on the aircraft into propulsive thrust. Stored energy can take a variety of forms: a spinning disk, a charged capacitor, a wound rubber band. But for most modern aircraft, onboard energy storage typically implies chemical energy in the form of fuel, or more recently chemical batteries. The first step of a propulsion system is therefore to convert chemical energy into mechanical work that can be then used to drive a propulsor. Two chemical reactions are of interest here. First is the well known combustion reaction:

$$C_xH_y + O_2 \longrightarrow CO_2 + H_2O \qquad \Delta H << 0 \tag{3.1}$$

For kerosene (aviation fuel), this reaction is:

$$2\ C_{12}H_{26} + 37\ O_2 \longrightarrow 24\ CO_2 + 26\ H_2O \qquad \Delta H = -7513\ \text{kJ} \tag{3.2}$$

Pure hydrogen can also be combusted:

$$2\ H_2 + O_2 \longrightarrow 2\ H_2O \qquad \Delta H = -483.6\ \text{kJ} \tag{3.3}$$

The most important byproduct of combustion is *heat*, commonly observed as flames. This heat can be used to drive any number of thermodynamic cycles, including the Brayton cycle that is used to operate most aircraft engines. Though the combustion reaction has been one of the most important in all of human history, production of CO_2 and also NO_x has caused dramatic harm to the planet. However, another chemical reaction has started to become just as important to civilization for converting chemical energy into useful work: the redox reaction. The redox reaction may not be as well known as combustion, but it is just as much a part of everyday life. The formation of rust, and the browning of fruits and vegetables are two such examples, but perhaps more relevant is that redox reactions power nearly all of the batteries in use today.

Consider again the hydrogen combustion reaction:

$$H_2 + \frac{1}{2}\ O_2 \longrightarrow H_2O \tag{3.4}$$

This can be broken down into the following half reactions:

$$H_2 \longrightarrow 2\ H^+ + 2\ e^- \tag{3.5}$$

$$\frac{1}{2}\ O_2 + 2\ H^+ + 2\ e^- \longrightarrow H_2O \tag{3.6}$$

The first half reaction is referred to as an *oxidization* reaction where the hydrogen atoms each lose an electron. The second half reaction is referred to as a *reduction* reaction where the oxygen atom will gain two electrons. In combustion, these two half reactions essentially occur simultaneously to compose the well known combustion equation (though chemical kinetics is not the focus of this work). But imagine if somehow these two reactions could be split up? The oxidation reaction could occur in one location, the electrons could be harvested and flowed through some electronic device to do useful work, and then the reduction reaction could be completed at a second location to finish the full reaction. This is the fundamental principle behind hydrogen fuel cells [7] (Figure 6).

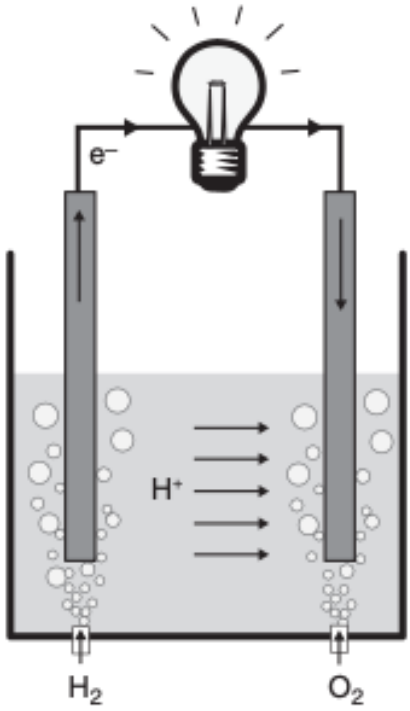


Figure 6: A simple fuel cell

3.3.2 Modeling Approach

From the perspective of the OpenConcept mission simulation, the fuel cell model is simply a box that takes in hydrogen fuel and outputs electrical power. Given the size and weight allocated to the fuel cell, a certain maximum power is available, and a throttle setting in the range [0,1] is passed from the mission simulator to specify what fraction of this maximum power is required to maintain flight at some given flight condition. If the required power exceeds the maximum power, then the OpenConcept optimizer will increase the allocated weight and size of the fuel cell and re-run the analysis.

There are two types of fuel cells considered in this work: Solid Oxide Fuel Cells (SOFCs) and Proton-Exchange Membrane (PEM) Fuel Cells. A detailed discussion of the physics behind each

type is left to the literature [7], but from a modeling standpoint the two are very similar. Four main steps exist for modeling both types of fuel cell. First, basic physical parameters must be computed based on the operating conditions of the fuel cell, namely the diffusivity of the relevant reactants in the relevant working mediums. Second, the theoretical maximum fuel cell efficiency must be computed. Third, the peak available power must be computed based on the size and operating parameters of the fuel cell. Finally, the fuel cell model must convert a given throttle setting to a fuel flow and a power output.

The key difference between SOFCs and PEMFCs is that SOFCs run at a much hotter temperature. SOFCs run so hot that all reactants and products exist in a gaseous state, and so the energy associated with phase conversions does not need to be taken into account. However, PEMFCs operate at temperatures where liquid water is present, and actually require liquid water to be present for the operation of the H^+ carrying electrolyte. For this reason, PEMFC modeling is significantly more complex.

Both models take in operating conditions pressure and temperature along with a given throttle setting, and produce outputs of a required fuel flow and a produced power.

Computing Diffusivity Hydrogen fuel cells operate primarily on the principle of diffusion. The high concentration of molecular hydrogen at the anode causes the hydrogen to diffuse through the fuel cell, kick-starting the redox reaction. On the cathode face, oxygen will be constantly absorbed, leading to a concentration gradient between the surface of the cathode and the rest of the air in the working volume. The oxygen must therefore diffuse through the nitrogen in the air in order to reach the cathode surface and allow the second half of the redox reaction to complete. In PEMFCs, liquid water is present throughout the entire fuel cell to enable the passage of hydrogen ions through the nafion electrolyte, and thus diffusion of both hydrogen and oxygen through water are necessary to compute as a part of the model.

The diffusivity of one medium in another medium depends on the temperature and pressure of the vessel containing the two media, along with the chemical properties of the media themselves. O'Hayre et. al. [7] provides the following expression for binary diffusivity:

$$D_{ij} = \frac{a}{p}\left(\frac{T}{\sqrt{T_{ci}T_{cj}}}\right)^{b}\left(p_{ci}p_{cj}\right)^{1/3}\left(T_{ci}T_{cj}\right)^{5/12}\left(\frac{1}{M_i}+\frac{1}{M_j}\right)^{1/2} \tag{3.7}$$

Relevant parameters are included in Table 17, Table 18 and Table 19.

Table 17: Constants for the diffusivity model when using pairs of gases (eg: H_2, O_2, N_2)

Constant	Value
a	2.745×10^{-4}
b	1.823

The model [7] is somewhat strange in that the assumed units are pressure in atmospheres, temperature in Kelvin, and the output is binary diffusion coefficient in (cm^2/s). Implementation in OpenConcept modifies the output to (m^2/s) using a division by 1e4.

Table 18: Constants for the diffusivity model when using a nonpolar gas (eg: H_2, O_2, N_2) and water (H_2O)

Constant	**Value**
a	3.640×10^{-4}
b	2.334

Table 19: Parameters for the diffusivity model

Substance	M	T_c	p_c
H_2	2.016 g/mol	33.3 K	12.8 atm
N_2	28.013 g/mol	126.2 K	33.5 atm
O_2	31.999 g/mol	154.4 K	49.7 atm
H_2O	18.015 g/mol	647.3 K	217.5 atm

Computing the Theoretical Thermodynamic Maximum Efficiency Just as a Carnot cycle has an upper bound on its theoretical efficiency, hydrogen fuel cells also have a limit on maximum efficiency based on foundational chemistry. A full discussion is left for the literature [7], but the model implemented here is as follows:

$$\Delta\hat{h}^0 = \Delta\hat{h}^0_{H_2O} - (\Delta\hat{h}^0_{H_2} + 0.5\Delta\hat{h}^0_{O_2}) \tag{3.8}$$

$$\Delta\hat{s}^0 = \Delta\hat{s}^0_{H_2O} - (\Delta\hat{s}^0_{H_2} + 0.5\Delta\hat{s}^0_{O_2}) \tag{3.9}$$

$$\Delta\hat{g} = \Delta\hat{h}^0 - T\Delta\hat{s}^0 \tag{3.10}$$

$$\varepsilon_{\text{thermo}} = \frac{\Delta\hat{g}}{\Delta\hat{h}^0_{H_2O(\ell)}} \tag{3.11}$$

The value $\Delta\hat{h}^0$ is the change in intrinsic enthalpy, $\Delta\hat{s}^0$ is the change in intrinsic entropy, and $\Delta\hat{g}^0$ is change in intrinsic Gibbs free energy. See the references [7] for a full discussion of these quantities, but relevant values can be found in Table 20

Table 20: Parameters for computing the thermodynamic efficiency of fuel cells

Chemical Species	$\Delta\hat{h}^0_f$	$\Delta\hat{s}^0_f$
H_2	0.0 kJ/mol	130.68 J/(mol·K)
O_2	0.0 kJ/mol	205.00 J/(mol·K)
H_2O(g)	-241.83 kJ/mol	188.84 J/(mol·K)
$H_2O(\ell)$	-285.83 kJ/mol	69.95 J/(mol·K)

Two different cases must be considered, the case where liquid water is produced and the case where gaseous water is produced. Since the condensation of water releases energy, values of $\Delta\hat{h}^0_{H_2O}$ and $\Delta\hat{s}^0_{H_2O}$ will be different depending on the phase of the water product. This model assumes that if the fuel cell operating temperature is greater than the boiling point of water (373.15 K), then gaseous water is produced, otherwise liquid water is produced. In practice, this essentially means that all SOFCs use the gaseous water value, while PEMFCs use the liquid water value.

When computing the thermodynamic efficiency, the higher heating value of water (-285.83 kJ/mol) should always be used. See O'Hayre et. al. [7] for a full discussion.

Computing the Peak Available Power Taking a step back, fuel cells are very similar to batteries in that they produce an electrical current by means of some chemical reaction. Just as batteries have some internal limits on how much power they can provide, fuel cells have similar limitations.

Perhaps the most intuitive limit of fuel cells is the result of Ohmic Losses, which are exactly the same as the internal resistance of a battery. The hydrogen ions passing through the fuel cell electrolyte cannot do so freely, and the resistance to their motion generate losses in the form of heat. As with batteries, Ohmic Losses in fuel cells are generally linearly proportional to the current being produced.

The second limit of fuel cells is also relatively intuitive: there is only so much hydrogen and oxygen that can be pumped through a fuel cell of a given area. As this upper limit is reached, the fuel cell will see a sharp decrease in efficiency, since so much energy is being spent just pumping large quantities of reactants through the cell. The losses associated with this physical limit are referred to as Mass Transport Losses. Mass transport dictates some upper limit on current per unit area (referred to as current density), which is typically between 1 and 10 A/cm^2 depending on fuel cell technology [7]. The nominal value in this work is taken to be 2 A/cm^2.

The last limit on fuel cells is relatively unintuitive. Consider the anode where significant numbers of hydrogen ions (H^+) are being generated. The anode quickly becomes saturated with hydrogen ions, which then must diffuse to the cathode to complete the reaction. Because of this hydrogen ion saturation, the rate of reaction at the anode grinds to a halt, significantly slowing down the chemical kinetics. However, taking the theoretical maximum voltage to be approximately 1.23 V [7], a small portion of this voltage can be sacrificed in the form of an electric field with reversed direction. This electric field applies a force to the positively charged hydrogen ions, accelerating the chemical reaction at the anode. This 'tax' associated with increasing the rate of reaction at the anode (and cathode) is referred to as an Activation Loss. A full discussion can be found in the references [7].

All three of these limits on fuel cell performance get worse as the current density increases, but each has a specific regime where it dominates the other two. Activation losses dominate at extremely low current densities, where current flow is low (hence ohmic losses are negligible) and reactant mass flows are also small (leading to negligible mass transport losses). At intermediate current densities, ohmic losses dominate, and at high current densities mass transport dominates. These three regions cause the plots of fuel cell efficiency vs. current density to have a very specific shape shown in Figure 7.

Note that for fuel cells, there is a direct relationship between voltage and efficiency. Since the ideal cell voltage (approximately 1.23 V) represents a cell with no losses [7], voltage is in essence a direct surrogate for efficiency. The two quantities are therefore often used interchangeably in the literature.

Given the unique shape of the voltage (ie efficiency) curve, there is a clear trade-off to be analyzed. Electrical power is computed as $P = IV$. At a current just greater than zero, voltage is as high as it can possibly be, but pulling high current will eventually drive the voltage to zero due to mass transport losses. There is some intermediate value for current where power will be maximized, as shown in Figure 8.

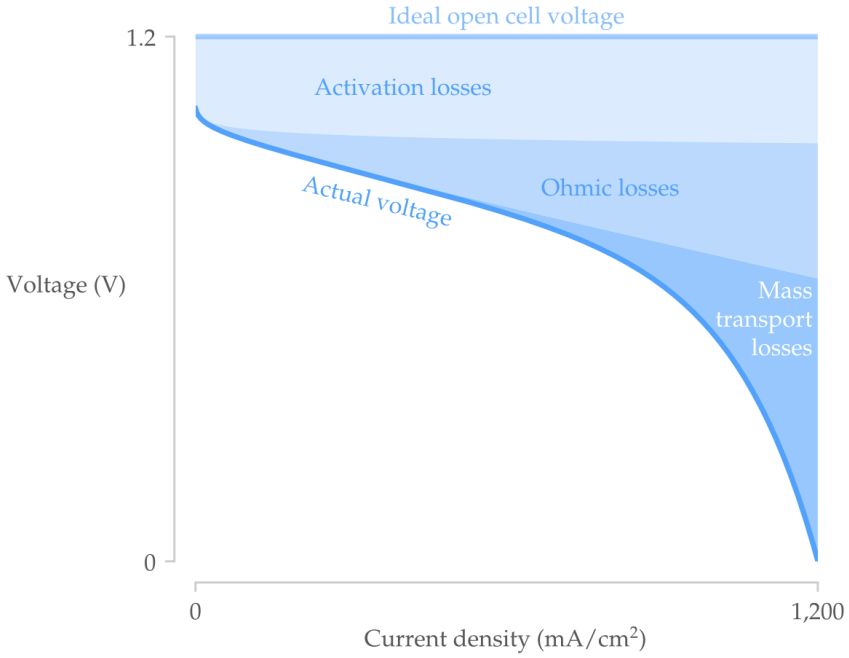


Figure 7: The breakdown of a fuel cell voltage (efficiency) curve (taken from [1])

For the purposes of aircraft performance analysis, this peak power represents full throttle, with all other throttle settings corresponding to some fractional current draw below this peak value. It is therefore necessary to compute the value of current density at this peak.

The full physics of fuel cell power are somewhat complex and left to the literature [7], but the relevant mathematics will be reproduced here. Our primary concern is developing an expression for area normalized power of the fuel cell:

$$p = jV \tag{3.12}$$

where p is the normalized power (eg W/cm^2), j is the current density (eg A/cm^2), and V is the cell voltage. As has been stated, the theoretical maximum for cell voltage is $V_{\text{thermo}} = 1.23$ V. Thus, voltage (V) can be computed as:

$$V = V_{\text{thermo}} - V_{\text{losses}} \tag{3.13}$$

We assert without proof that the voltage of a SOFC can be computed as [7]:

$$V = E_{\text{thermo}} - j\frac{t_M T}{A_{\text{SOFC}} e^{-\Delta G_{\text{act}}/(RT)}} - \frac{RT}{4\alpha F}\ln\left[\frac{j}{j_L}\frac{4FD^{\text{eff}}_{O_2,N_2}p_{\text{atm}}}{t_C RT j_0(1-\frac{j}{j_L})}\right] \tag{3.14}$$

where the first term is E_{thermo}, the second term is ohmic losses, and the third term is mass transport and activation losses at the cathode (which with slower kinetics can be assumed to dominate the fuel cell reaction).

For a PEMFC, the analysis is somewhat more complex. Unlike SOFCs, where ohmic losses can be assumed constant throughout the electrolyte, PEMFCs use a nafion electrolyte that must be saturated with water during operation. Since the electrolyte has a steady stream of positively

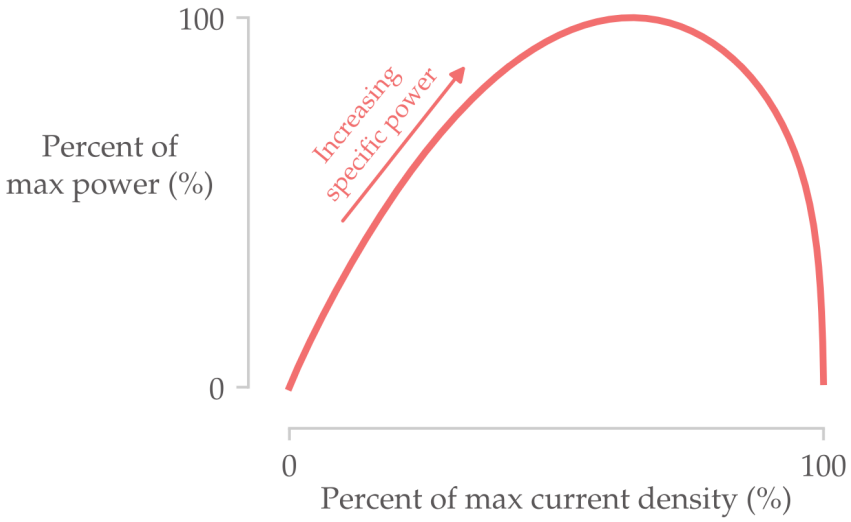


Figure 8: A typical fuel cell power curve (taken from [1])

charged hydrogen ions flowing through it from anode to cathode, the polar water molecules will be 'dragged' from anode to cathode, leading to a concentration gradient. When current density is low the gradient will be small, and when current density is high the gradient will be relatively large. As a result, it is necessary to perform an integral over the length of the electrolyte to compute the effective resistivity of the nafion electrolyte.

Computing the effective resistivity of nafion essentially requires the solution of a linear system for two critical parameters, α^* and C:

$$a_{1,1} = 4.4 + \frac{p_A}{p_{SAT}} \frac{t_A j RT}{2F p_A D^{\text{eff}}_{H_2,H_2O}} \tag{3.15}$$

$$a_{1,2} = 1.0 \tag{3.16}$$

$$b_1 = 14 \frac{p_A}{p_{SAT}} x_{H_2O} \tag{3.17}$$

$$K = \frac{t_C j RT}{4F p_C D^{\text{eff}}_{O_2,H_2O}} \tag{3.18}$$

$$a_{2,1} = 4.4 + (4 \frac{p_C}{p_{SAT}} K) \tag{3.19}$$

$$a_{2,2} = e^{0.000598 j t_M / D_\lambda} \tag{3.20}$$

$$b_2 = 10.0 + 4 \frac{p_C}{p_{SAT}} (x_{H_2O} + K) \tag{3.21}$$

$$\alpha^* = (b_1 - a_{1,2} b_2 / a_{2,2}) / (a_{1,1} - a_{1,2} a_{2,1} / a_{2,2}) \tag{3.22}$$

$$C = (b_2 - a_{2,1} \alpha^*) / a_{2,2} \tag{3.23}$$

Which are used to compute the resistivity integral:

$$\lambda = 4.4 \alpha^* + C e^{0.000598 j z / D_\lambda} \tag{3.24}$$

$$\sigma(z) = (0.005193 \lambda - 0.003261) e^{1268 (\frac{1}{303} - \frac{1}{T})} \tag{3.25}$$

$$ASR_m = \int_0^{t_M} \frac{dz}{\sigma(z)} \tag{3.26}$$

Resulting in the following equation for voltage:

$$V = E_{\text{thermo}} - j \cdot ASR_m - \frac{RT}{4\alpha F} \ln \left[\frac{j}{j_L} \frac{4FD^{\text{eff}}_{O_2,N_2} p_{\text{atm}}}{t_C RT j_0 (1 - \frac{j}{j_L})} \right] \tag{3.27}$$

where as before the first term is E_{thermo}, the second term is ohmic losses, and the third term is mass transport and activation losses at the cathode (which with slower kinetics can be assumed to dominate the fuel cell reaction). Note that unit bookkeeping may be somewhat tricky, as it is often more convenient to work with current densities in A/cm^2 instead of the standard base units A/m^2 assumed by the model. Also note that the values for pressure of the anode (p_A) and cathode (p_C) are assumed to be the same as the pressure of the fuel cell as a whole (p).

A few loose ends remain. First, diffusion in fuel cells is typically occurring through some solid, which results in a different diffusivity than the one computed in the previous section. This effective diffusivity correction depends on temperature, and thus is different for the two varieties of fuel cell. For high temperature SOFCs, the correction is:

$$D^{\text{eff}}_{i,j} = D_{i,j} \frac{\varepsilon}{\tau} \tag{3.28}$$

and for lower temperature PEMFCs:

$$D^{\text{eff}}_{i,j} = \varepsilon^{\tau} D_{i,j} \tag{3.29}$$

Furthermore, though the thickness of the cathode is likely to be set by structural limits of current fuel cell technology, the model here instead chooses to implicitly set t_C based on a limit current j_L:

$$t_C = \frac{4FD^{\text{eff}}_{O_2,N_2}}{j_L} \frac{x_{O_2} p}{RT} \tag{3.30}$$

Also required for the PEMFC model is the vapor saturation pressure, which is computed via the Buck equation:

$$p_{SAT} = 611.21 \exp \left(18.678 - \frac{(T - 273.15)^2}{234.5(T - 16.01)} \right) \tag{3.31}$$

which takes in temperature in Kelvin and returns vapor saturation pressure in Pascals. All that now remains are the assumed values of the parameters, which are provided in Tables 21 and 22.

The above presents a full model for computing area normalized power of a fuel cell as a function of temperature, pressure, and current density for both SOFCs and PEMFCs. Maximum power obtained by a simple sweep over a finely discretized grid of current densities, and the maximum power current density is designated as $j_{\max}$. Future work could potentially implement a more intelligent calculus based approach.

Table 21: Parameters for SOFC modeling

Parameter	Value	Description
E_{thermo}	1.06 V	Maximum theoretical voltage
t_M	20×10^{-6} m	Electrolyte membrane thickness
A_{SOFC}	9×10^{7} K/(Ω·m)	Electrolyte constant
ΔG_{act}	1×10^{5} J/mol	Electrolyte activation energy
R	8.314 J/(mol·K)	Gas constant
α	0.5	Transfer coefficient
F	96485.34 C/mol	Faraday constant
p_{atm}	101325 Pa	Atmospheric pressure
j_L	2.0 A/cm^2	Limit current density (needs conversion)
j_0	0.1 A/cm^2	Exchange current density (needs conversion)
τ	1.5	Tortuosity
ε	0.4	Porosity
x_{O_2}	0.19	Oxygen mole fraction in air

Table 22: Parameters for PEMFC modeling

Parameter	Value	Description
t_A	350×10^{-6} m	Anode thickness
R	8.314 J/(mol·K)	Gas constant
x_{H_2O}	0.1	Cathode water mole fraction
F	96485.34 C/mol	Faraday constant
t_M	125×10^{-6} m	Electrolyte membrane thickness
D_λ	3.81×10^{-10} m^2/s	Diffusivity of water in nafion
E_{thermo}	1.22 V	Maximum theoretical voltage
α	0.5	Transfer coefficient
j_L	2.0 A/cm^2	Limit current density (needs conversion)
p_{atm}	101325 Pa	Atmospheric pressure
j_0	0.1 A/cm^2	Exchange current density (needs conversion)
τ	1.5	Tortuosity
ε	0.4	Porosity
x_{O_2}	0.19	Oxygen mole fraction in air

Linking Fuel Cell Analysis to Aircraft Performance The previous section outlined a method for obtaining the area scaled power of solid oxide fuel cells and proton-exchange membrane fuel cells, taking in inputs of fuel cell pressure, temperature, and current density. Given now that a current density for maximum power has been computed, throttle setting can be defined as:

$$x_{\text{throttle}} = \frac{j}{j_{\max}} \tag{3.32}$$

And so, for a given throttle setting, area scaled power can now be computed.

The aircraft model must also store a design variable representing the total area of the fuel cell, which sets the maximum dimensioned power available for a given fuel cell design:

$$P_{\max} = j_{\max} V A_{\text{FC}} \tag{3.33}$$

However, most fuel cells produce voltages too low to be practical, or else are combined in a stack with a non-standard output voltage. There must be a DC-DC conversion, which has an assumed efficiency of 0.9 for this work, making the equation for maximum power:

$$P_{\max} = \eta_{DC} j_{\max} V A_{\mathrm{FC}} \tag{3.34}$$

The weight of the fuel cell is computed from this area variable multiplied by a constant weight per unit area:

$$W_{\mathrm{FC}} = w_{\mathrm{FC}} A_{\mathrm{FC}} \tag{3.35}$$

The mass flow of hydrogen (H_2) fuel consumed by the fuel cell can be computed as:

$$\dot{m}_{H_2} = \frac{j}{2F} A_{\mathrm{FC}} \tag{3.36}$$

These equations complete the model, which takes in:

- Pressure
- Temperature
- Throttle Setting
- Fuel Cell Area

and outputs:

- Available Power
- Hydrogen Flow Rate
- Fuel Cell Mass

3.3.3 Model Trends

PEMFCs are More Sensitive to Pressure than SOFCs Sweeping the model over a variety of pressures shows that PEMFCs are far more sensitive to pressure variations than SOFCs (Figure 9). For aircraft design applications this is of significant concern, since fuel cells must operate at altitude. One solution is to pressurize the PEMFC chamber, essentially 'turbocharging' the fuel cell. However, compression comes at the additional cost of weight and power and the favorability of this trade is unclear.

SOFCs Work Best Running Very Hot SOFC fuel cells produce more power and are more efficient when running at extremely hot temperatures (Figure 10). Maximum performance is seen at 1000°C, which is near the temperatures experienced by the first stage of the high pressure turbine in a conventional jet engine (approximately 1400K).

PEMFCs Work Best Around 40°C In contrast to SOFCs, PEMFCs have a clear optimal temperature between 35°C and 40°C (Figure 11).

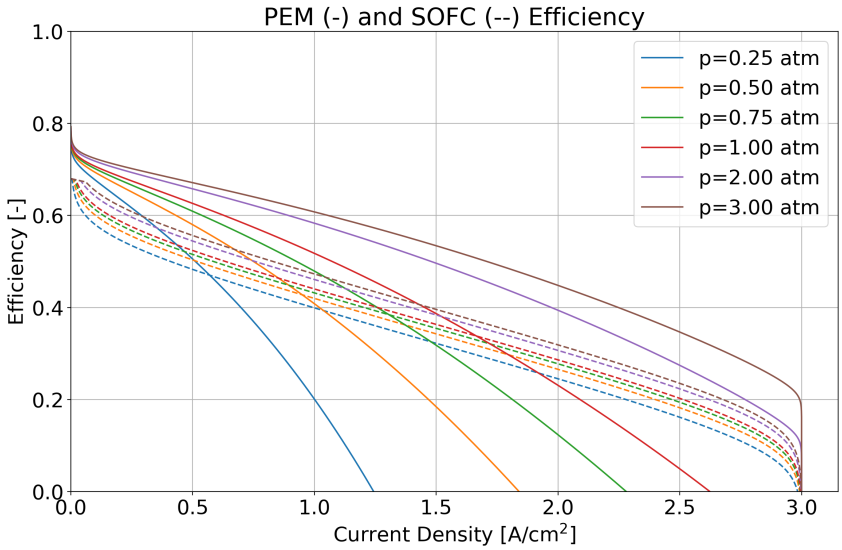
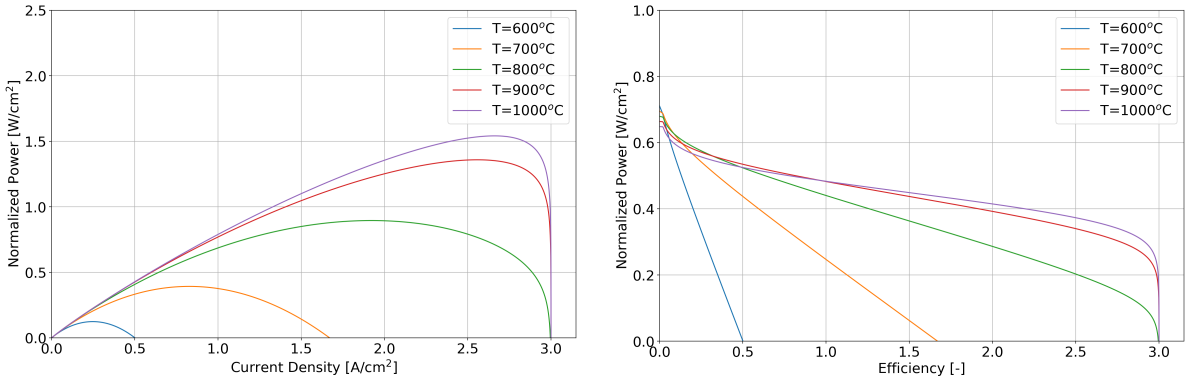


Figure 9: Variation of pressure for both SOFCs and PEMFCs



(a) Fuel cell power

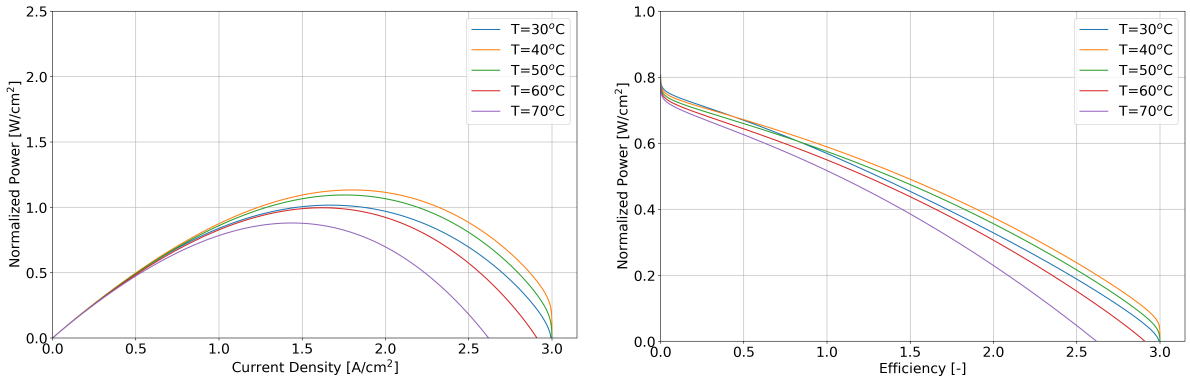
(b) Fuel cell efficiency

Figure 10: Study of SOFCs with varying temperature

There is a Trade-Off Between Fuel Cell Weight and Fuel Cell Efficiency If an assumption is made for a mass per unit area of a fuel cell, along with a fixed run-time, it is possible to compute the total mass per unit power of the system:

$$\frac{m_{\text{FC}} + m_{\text{H}_2}}{P} = \frac{w_{\text{FC}} + \frac{j}{2F} t_{\text{run}}}{jV} \tag{3.37}$$

For a fixed output power, a very large fuel cell will draw a very low current density, resulting in maximum efficiency. While heavy, this may be desirable for extremely long running applications (ex long-haul aircraft). However, a smaller fuel cell will save fixed weight, but the higher current density will move the operating point to a much lower efficiency. This may be desirable for short duration applications like eVTOL or regional aircraft. Optimal selections (ie minimum combined masses) are easily identifiable in Figure 12.



(a) Fuel cell power

(b) Fuel cell efficiency

Figure 11: Study of PEMFCs with varying temperature

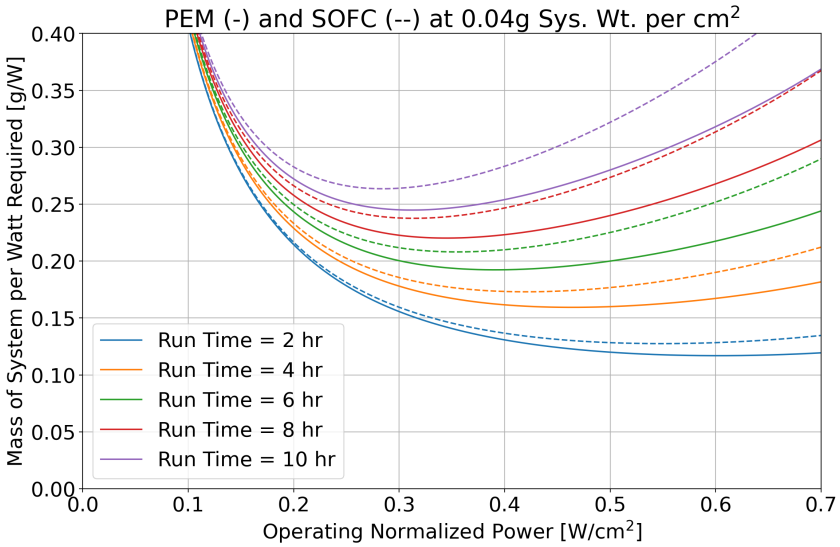


Figure 12: Trade-off between fuel cell size and efficiency, large fuel cells are towards the left of the chart, smaller fuel cells towards the right

3.4 Strayton Power Generator

Traditional aircraft turbomachines utilize the Brayton cycle to produce both power and thrust. In the case of a turboprop or turbofan engine, the Brayton power generating core is primarily tasked with generating shaft power which turns the primary propulsor, whereas a turbojet engine uses expanded air from the power generator to propel the aircraft forward.
The Brayton cycle can be broken out into four distinct stages:

1. Adiabatic Compression
2. Isobaric Heat Addition
3. Adiabatic Expansion
4. Isobaric Heat Rejection

This cycle is often represented on a T-s diagram as shown in Figure 13.

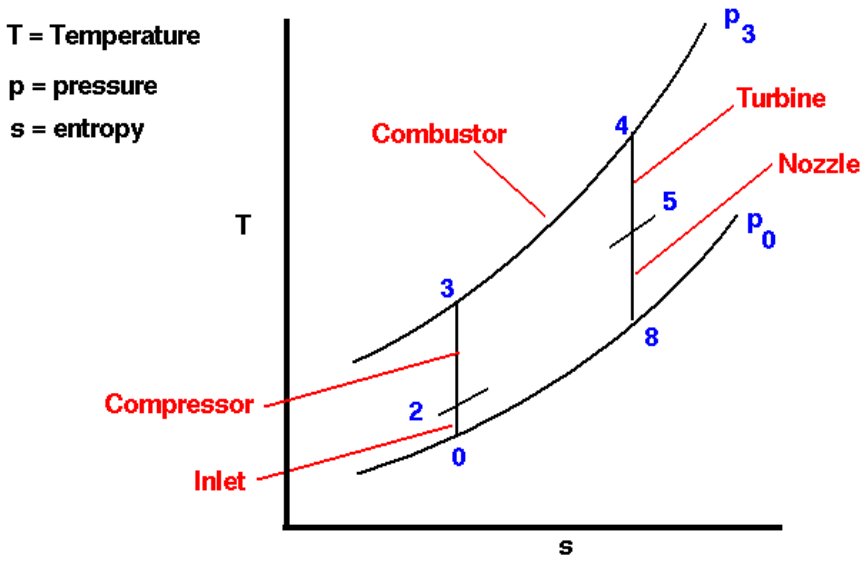


Figure 13: A T-s Diagram representing the Brayton Cycle

For a typical open cycle aircraft engine, the final stage of isobaric heat rejection takes place in the wake of the aircraft, where it dissipates into the atmosphere. Given the significant investment of energy to heat up this air, this dissipation is a significant source of wasted energy. The Regenerative Brayton Cycle captures some or all of this heat rejection, and transports the heat back to the isobaric heat addition stage of the cycle, essentially boosting the heat addition so that less fuel is required to raise the working fluid to its peak temperature. The T-s Diagram for this cycle appears in Figure 14.

In practice, the regenerative Brayton cycle is not implemented on aircraft engines because the extra weight and complexity of the regenerative systems negates the efficiency improvements that come from the regeneration. In response to this, recent work by Dyson [2] proposed a novel power generator that utilizes a series of four closed cycle Brayton engines, where rejected heat is recovered for use in the next stage. Further boosting this closed cycle is a Stirling acoustic engine that serves as a

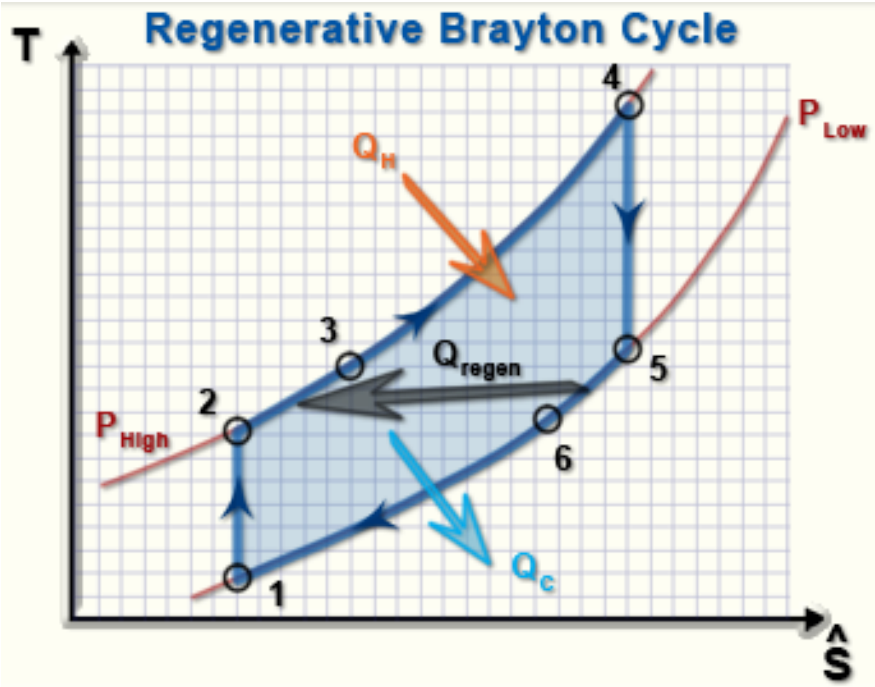


Figure 14: A T-s Diagram representing the Brayton Cycle

topping cycle to the Brayton quad, giving rise to the term 'Strayton' to describe this combined cycle.

The Strayton generator can be conceptualized as a black-box that converts heat to electrical energy. Unlike a traditional turbomachine, where the heat addition is done by injecting fuel into the working fluid, the closed cycle Strayton generator separates the heating element from the working fluid. As a simple mental picture, envision a sealed pipe of cold working fluid coiled around a heat source. When fluid enters the coils, it is at the lower working temperature, but when it leaves the coils, the working fluid has reached its peak operating temperature (ideally the temperature of the heat source). Because of this separation, the heat source could be nearly anything. Dyson [2] proposes basic combustion chambers and nuclear reactors among other sources. One interesting piece of future work would be to consider driving a Strayton engine with a hydrogen fuel cell, which naturally generates significant waste heat when generating electricitiy, essentially creating a combined cycle like that proposed by Bradley [8]. However, this work only considers a standard combustion chamber as the heat source, optionally powered by either traditional kerosene or hydrogen.

From the perspective of the currently formulated aircraft design problem, the Strayton power plant is merely a black-box of a certain weight that converts a fuel flow rate into an output power given some operating efficiency. Therefore, the Strayton model need only consist of two numbers: specific power (ie, power generated by the Strayton generator per unit mass) and efficiency (ie, power of fuel in divided by power of electrical energy out). For this work, a fixed specific power of 6 kW/kg is assumed. The efficiency model is taken straight from Dyson [2], but has been implemented in OpenMDAO for use with the larger aircraft design framework. The full Strayton model is as follows.

The model takes in as inputs the mass of the Strayton power generator and the throttle setting, which is used to fly the mission profile. From the mass input, the maximum available power of the

Strayton engine is computed as:

$$P_{\max} = m_{\text{Strayton}} \left(6000 \frac{\text{W}}{\text{kg}} \right) \tag{3.38}$$

The power being drawn from the engine is then computed as:

$$P_{\text{out}} = x_{\text{throttle}} P_{\max} \tag{3.39}$$

where x_{throttle} is a float in range [0,1] indicating the position of the throttle lever. The fuel flow required by the Strayton generator can be computed as:

$$\dot{f}_{\text{fuel}} = \frac{Q_{\text{required}}}{U'_{\text{fuel}}} \tag{3.40}$$

where Q_{required} is the heat required to power the Strayton cycle, and U_{fuel} is the internal energy of the fuel (142 MJ/kg for hydrogen and 43.02 MJ/kg for kerosene). The heat required by the Strayton cycle is related to the power out at the given throttle setting, and the efficiency of converting the heat from the fuel into power, ie:

$$Q_{\text{required}} = \frac{P_{\text{out}}}{\eta_{\text{total}}} \tag{3.41}$$

The value η_{total} is computed using the Dyson model [2], but a full derivation is beyond scope here. The value of η_{total} will depend on design decisions for the Strayton engine, which for the purposes of this work are assumed fixed, but are recorded in Table 23[1]. The relevant equations are as follows:

$$C = r^{\frac{R}{c_{p_c} \eta_{p_c}}} - 1 \tag{3.42}$$

$$E_4 = 1 - \left(r(1 - 0.25 p_{\text{loss}}) \right)^{-\frac{R}{c_{p_e}} \eta_{p_e}} \tag{3.43}$$

$$\dot{W}' = 4 \left(\frac{\dot{m}_e}{\dot{m}_c} \right) \left(\frac{c_{p_e}}{c_{p_c}} \right) E_4 T' - 4C + 6C^2(\varepsilon_i - 1) - 4C^3(\varepsilon_i - 1)^2 + C^4(\varepsilon_i - 1)^3 \tag{3.44}$$

$$\dot{Q}' = \frac{\dot{m}_e c_{p_e}}{\dot{m}_c c_{p_c}} \left(-(1 + C)(-1 + C(\varepsilon_i - 1))^3(\varepsilon_x - 1) + T' - \varepsilon_x T' + E_4(\varepsilon_x + 3)T' \right) \tag{3.45}$$

$$\eta_{\text{total}} = \frac{\dot{W}'}{\dot{Q}'} \tag{3.46}$$

Note that mass flow through the compressor ($\dot{m}_c$) and mass flow through the turbine (ie. expander, $\dot{m}_e$) are assumed equal since no fuel is injected into the working fluid. The specific heat capacity of Helium can also assumed to be constant (ie, $c_{p_c} = c_{p_e}$) simplifying these expressions to:

$$C = r^{\frac{R}{c_{p_c} \eta_{p_c}}} - 1 \tag{3.47}$$

$$E_4 = 1 - \left(r(1 - 0.25 p_{\text{loss}}) \right)^{-\frac{R}{c_{p_e}} \eta_{p_e}} \tag{3.48}$$

$$\dot{W}' = 4E_4 T' - 4C + 6C^2(\varepsilon_i - 1) - 4C^3(\varepsilon_i - 1)^2 + C^4(\varepsilon_i - 1)^3 \tag{3.49}$$

$$\dot{Q}' = \left(-(1 + C)(-1 + C(\varepsilon_i - 1))^3(\varepsilon_x - 1) + T' - \varepsilon_x T' + E_4(\varepsilon_x + 3)T' \right) \tag{3.50}$$

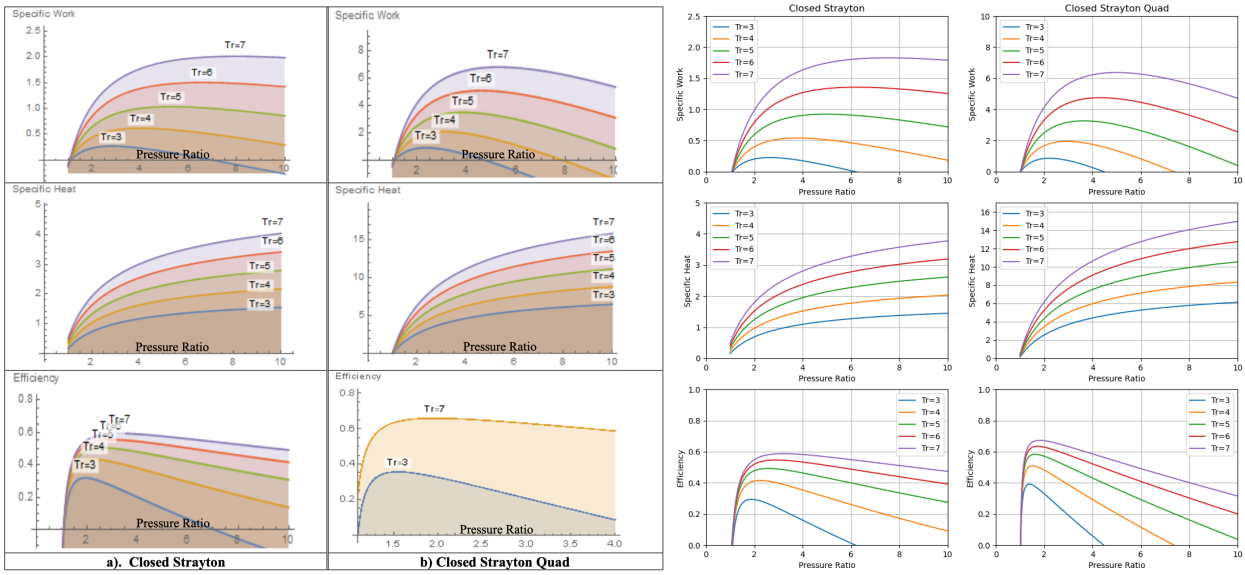
$$\eta_{\text{total}} = \frac{\dot{W}'}{\dot{Q}'} \tag{3.51}$$

These equations complete the model.
The OpenMDAO model was compared against data reported by Dyson [2] as validation, with results available in Figure 15.

[1]The Dyson [2] paper assumed a working fluid of He-Xe, but this model assumes pure He and obtains similar results

Table 23: Parameters for the Strayton model

Parameter	Value	Description
r	1.9	Compressor pressure ratio
T'	7.0	Brayton Temperature Ratio (T_{t_4}/T_{t_1})
c_{p_c}	5192.6 J/(kg K)	Specific heat capacity for fluid (Helium) in the compressor
c_{p_e}	5192.6 J/(kg K)	Specific heat capacity for fluid (Helium) in the turbine
R	2076.9 J/(kg K)	Gas constant for the working fluid (Helium)
η_{p_c}	0.85	Efficiency of the compressor
η_{p_e}	0.85	Efficiency of the turbine
p_{loss}	0.05	Ratio of pressure losses ($\Delta p_{\text{losses}}/p$)
ε_x	0.9	Recovery efficiency
ε_i	0.9	Interstage recovery efficiency
U'_{fuel_H}	142 MJ/kg	Specific internal energy of hydrogen
U'_{fuel_K}	43.02 MJ/kg	Specific internal energy of kerosene



(a) The original model (from [2])

(b) The OpenMDAO Model

Figure 15: Comparison between the Strayton model from [2] and the OpenMDAO model created for the aircraft design case studies

4 Case Study: ATR72–600

In this section the different retrofit of the ATR72-600 are presented. New propulsion chains data are detailed in terms of weight, power and efficiency. At the end of each section, the entire aircraft model performance is presented in a table, with power plant weight, OEW, fuel used and TOW comparison to the baseline model.

4.1 Strayton Kerosene

The first propulsion retrofit is done for the Strayton engine with kerosene combustion. The changes concern the propulsion chain only. The chain is now composed of a main Strayton engine which produces electric power for two superconducting motors (SCM), each placed at the former position of the turboprops. The SCM are coupled with two propellers which remain the exact same as for the baseline model. The Table 24 presents the detail of each element weight. As no 2MW electric motor has been developed yet for a power, we assume that its weight is equal to the one of a turboprop. We also consider that the engine systems weights (misc) remain the same for the retrofit, even if there are not the exact same elements. These are two very pessimistic assumptions. Luckaczyk and al [9] present a 20kW/kg power-to-weight ratio curve for future Super Conducting Motors, when the electric motors of the model only have 3.4kW/kg. In a higher fidelity model these assumptions could be re-evaluated.

Table 24: ATR72–600 Strayton-kerosene propulsion weight data

	Strayton (1)	Motors (2)	Fans (2)	Misc	Total
Mass (kg)	680	1098	414	414	2728

The TOW mass breakdown is given in Figure 16. Compared to the baseline model the Strayton engine is lighter than the two turboshafts but the two additional electric motors which make the overall powerplant 39% heavier as shown in the Table 26. This penalty extends to gain in the OEW.

The propulsion data is detailed in Table 25. The overall efficiency of the chain is two times higher than the baseline model (0.48 vs 0.24). This massive gain implies a 50% fuel block reduction as mentioned in Table 26. Despite a mass gain for the OEW, the gain for the block fuel limits the TOW mass penalty at 1%.

Table 25: ATR72–600 Strayton-kerosene propulsion data

	Strayton	Motor	Fan	Total
Power (MW)	4.1	1.85	1.48	
Efficiency	0.67	0.9	0.8	0.48
Power-to-weight ratio (kW/kg)	6	3.4		

4.2 Hydrogen Turboprop Retrofit

The Figure 18 shows the new mass breakdown of the model after replacing the kerosene combustion by hydrogen combustion. The main change is in the payload since 1/3 of the passenger rows have been deleted. Fewer passengers also means fewer seats, less oxygen, hence the percentage change in the equipment. There is a significant change in the structure since the liquid hydrogen tanks

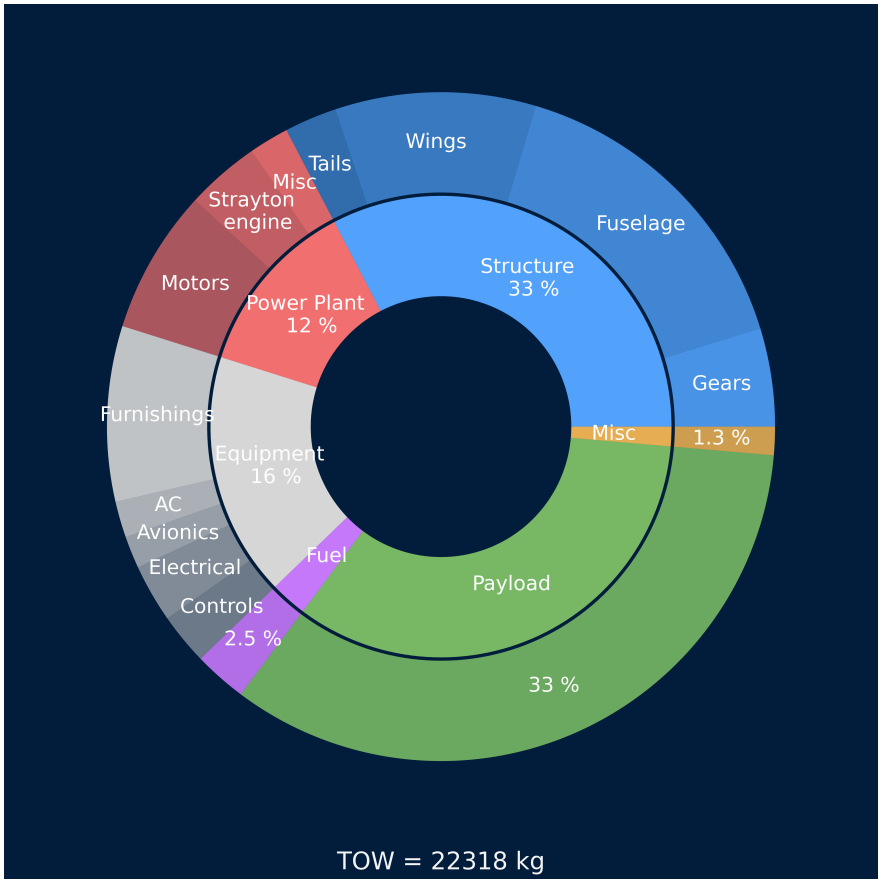


Figure 16: TOW mass breakdown for Kerosene Strayton model

Table 26: Strayton retrofit performances

	Kerosene turboprop	Strayton retrofit	Savings
Power plant weight (kg)	1963	2728	-39%
OEW (kg)	13603	14359	-5.6%
Fuel used (kg)	1113	559	50.22%
TOW (kg)	22117	22318	-1%

replace the kerosene tanks. These new tanks have a radius equal to that of the fuselage, their length is optimized, and they are placed at the back of the fuselage as shown on Figure 17. This standard length of 2m, will be kept for all the hydrogen retrofits no matter the volume of the block fuel.

The wings do no longer contain tanks but we do not consider any change in their structure. The propulsion chain remains the same as for the baseline model presented in section 3.3.4 and we do not consider any engine systems change. The block fuel has been roughly divided by three between the baseline and retrofit because the specific energy of the hydrogen is of 142MJ/kg compare to 46MJ/kg for kerosene.

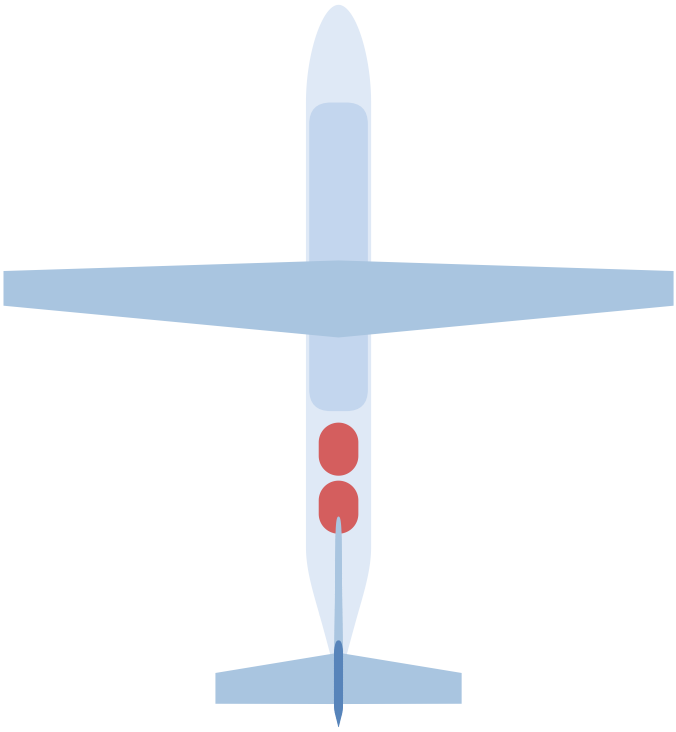


Figure 17: ATR72–600 hydrogen tanks

4.3 Strayton Retrofit

For this retrofit we take the precedent hydrogen turboprop propulsion baseline and we switch the propulsion chain to a Strayton engine with two SuperConducting Motors as in section 5.1.1. The propulsion data are presented in Table 27 and Table 28. Since the TOW for this retrofit is lighter than for the kerosene Strayton, the maximum power needed, at take-off, is lower. The Strayton engine for this model is then smaller. The assumptions concerning the electric motors and the engine systems remain the same as before: no changes compared to the turboprop elements weight. The efficiencies remain the same as for the previous Strayton retrofit.

Table 27: ATR72–600 Strayton-hydrogen propulsion weight data

	Strayton (1)	Motors (2)	Fans (2)	Misc	Total
Mass (kg)	540	1098	414	414	2728

Table 28: ATR72–600 Strayton-hydrogen propulsion data

	Strayton	Motor	Fan	Total
Power (MW)	3.24	1.46	1.17	
Efficiency	0.67	0.9	0.8	0.48
Power-to-weight ratio (kW/kg)	6	3.4		

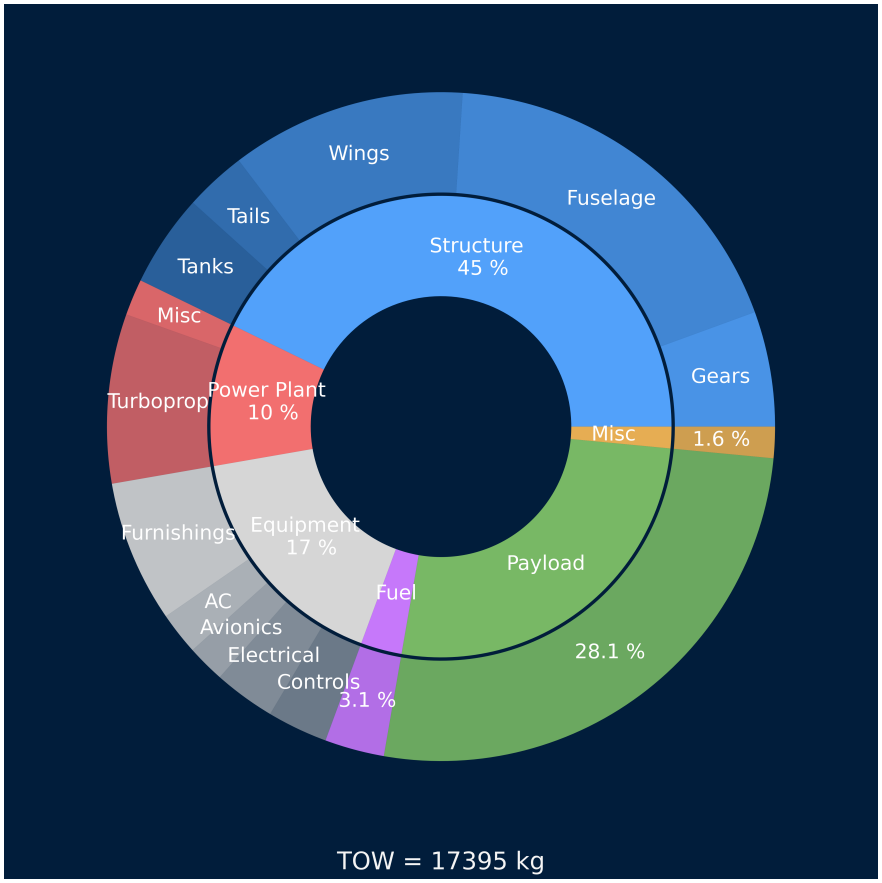


Figure 18: TOW Hydrogen model

Figure 19 presents the TOW mass breakdown of this new retrofit. Compared to the hydrogen turboprop baseline, this model has the same payload, structure and equipment. The propulsion percentage is slightly higher since the Strayton engine mass is added to the baseline power plant overall weight.

The Table 29 presents the comparative performance between hydrogen turboprop baseline and Strayton hydrogen retrofit. The pessimistic assumptions about the electric motors and engine systems have an impact on the power plant weight penalty which extends to a OEW penalty. The Strayton propulsion chain is highly efficient and the fuel used is divided by 2 compared to the turboprop baseline. This reduces the TOW penalty to 2%.

Table 29: Strayton hydrogen retrofit performance

	Hydrogen turboprop	Strayton with Hydrogen	Savings (%)
Power plant weight (kg)	1849	2152	-16.4
OEW (kg)	11973	12502	-4.4
Fuel used (kg)	482	226	46.9
TOW (kg)	17340	17693	-2.0

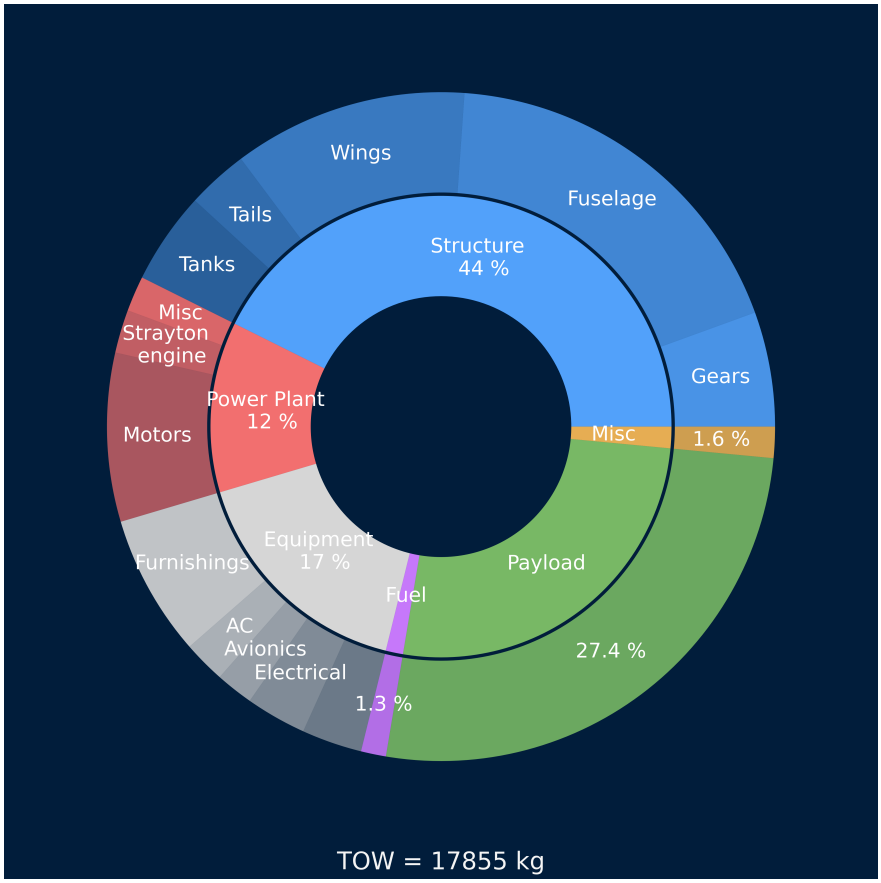


Figure 19: TOW Hydrogen Strayton model

4.4 Fuel Cells Retrofit

For this retrofit we take the hydrogen turboprop baseline and switch the propulsion chain to two fuel cells providing electric power to two SCM and propellers. The Figure 20 presents the TOW mass breakdown. Compared to the baseline, the hydrogen tanks, the structure, the equipment, the payload remain the same. We suppose that the fuel cells are placed under the wings, next to the electric motors. Despite their very important weight we do not consider any additional weight for the wings structure. The two electric motors are supposed to weight the same than the two turboprops from the baseline. Table 30 present each element weight in the propulsion chain. Overall, the power plant weight has been multiplied by four between baseline model and fuel cells retrofit.

Table 30: ATR72–600 fuel cells propulsion weight data

	Fuel cells	Motors	Fans	Misc	Total
Mass (kg)	5859	1098	414	418	7803

As shown on Table 31, this propulsion chain is roughly 20% more efficient than the baseline hence the fuel economy presented in the results Table 32. The power plant has a massive weight penalty which extends to a OEW penalty. Despite the save in the block fuel, the TOW of the retrofit remains significantly higher for the fuel cells retrofit.

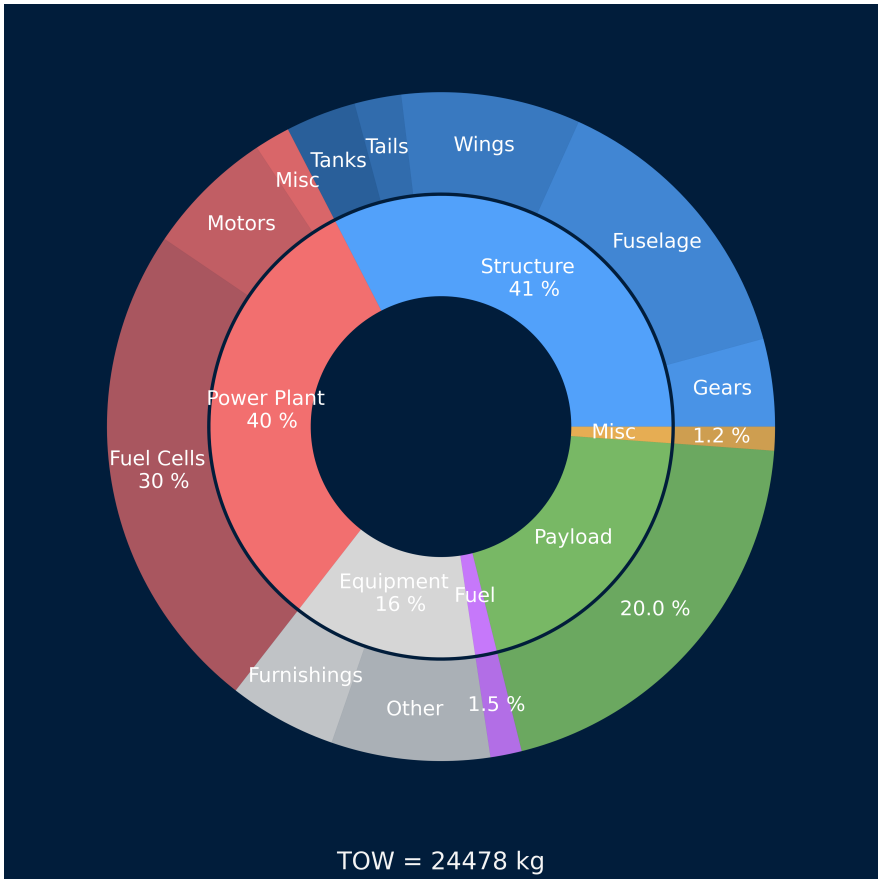


Figure 20: TOW fuel cells model

Table 31: ATR72–600 fuel cells propulsion data

	Fuel cells	Motors	Fans
Mass (kg)	2930	549	414
Power (MW)	2.2	2	1.6
Efficiency	0.6–0.8	0.9	0.8

Table 32: Fuel cells retrofit performance

	Hydrogen turboprop	Fuel cells	Savings
Power plant weight	1849 kg	7803 kg	-322 %
OEW	11973 kg	19222 kg	-60.5 %
Fuel used	482 kg	371 kg	23 %
TOW	17340 kg	24478 kg	-41.2 %

4.5 Global Comparison

As mentioned in previous sections, the massive loss of payload for the hydrogen retrofit would make any comparison with kerosene retrofit irrelevant. However in Table 33 the fuel per passenger-mile metric is calculated for all the retrofits. The more economic retrofit is the Hydrogen-Strayton and the worse is the kerosene turboprop baseline. Despite the massive loss of passengers for hydrogen retrofit, the block fuel economy, is sufficient to compensate it and make this technology more

profitable than kerosene turboprop. The pessimistic assumptions concerning the efficiency and the power-to-weight ratio of the electric motors for Strayton and fuel cells retrofit make the numbers worse than what they could be. The fuel cells retrofit seems to be competitive with Strayton technology but the actual integration of such massive power plant will be a challenge.

Table 33: Fuel per passenger-mile (lbs/nmi)

H2 Strayton	Fuel cells	Ker. Strayton	H2 turbopr.	Ker. turbopr.
0.015	0.0254	0.0371	0.0409	0.0852

5 Case Study: B737–800

In this section the different retrofit of the B737–800 are presented. New propulsion chains data are detailed in terms of weight, power and efficiency. At the end of each section, the entire aircraft model performance is presented in a table, with power plant weight, OEW, fuel used and TOW comparison to the baseline model.

5.1 Strayton Kerosene Retrofit

The only retrofit done for the B737–800 is a Strayton kerosene propulsion chain. For this retrofit the turbofans are replaced with two super conducting motors and a main Strayton engine placed at the back of the fuselage provides them electric power. The Super Conducting Motors are equipped with two ducted fans, from which the numerical model has been presented in section 3.3.4. Table 34 presents in detail the propulsion weight data for this model.

Table 34: B737–800 Strayton-kerosene propulsion weight data

	Strayton (1)	Motors (2)	Fans (2)	Misc	Total
Mass (kg)	3910	2225	300	1311	9590

Figure 21 presents the TOW mass breakdown for this retrofit. Compared to the baseline the only change concerns the power plant weight. The turbofans are now replaced by the two motors and the Strayton engine. The structure, payload and equipment weight remain the same. The block fuel is significantly smaller thanks to a higher efficiency of the Strayton propulsion chain.
The performance of the retrofit model are presented in Table 36. The power plant weight is heavier due to the pessimistic assumptions made on the power-to-weight ratio for the electric motors. This penalty extends to a OEW penalty. However the better efficiency of the propulsion chain reduces the block fuel of a third. This gain extends ends up in an overall efficiency for the TOW.

Table 35: B737–800 Strayton-kerosene propulsion data

	Strayton	Motor	Fan	Total
Power (MW)	19.2	8.6	6.9	
Efficiency	0.7	0.9	0.8	0.504
Power-to-weight ratio (kW/kg)	6	3.8		

Table 36: Strayton kerosene retrofit performances

	Kerosene turboprop	Strayton retrofit	Savings
Power plant weight	5593 kg	9590 kg	-71.46%
OEW	41748 kg	45240 kg	-8.36%
Fuel used	15979 kg	10829 kg	32.23%
TOW	78348 kg	75718 kg	3.36%

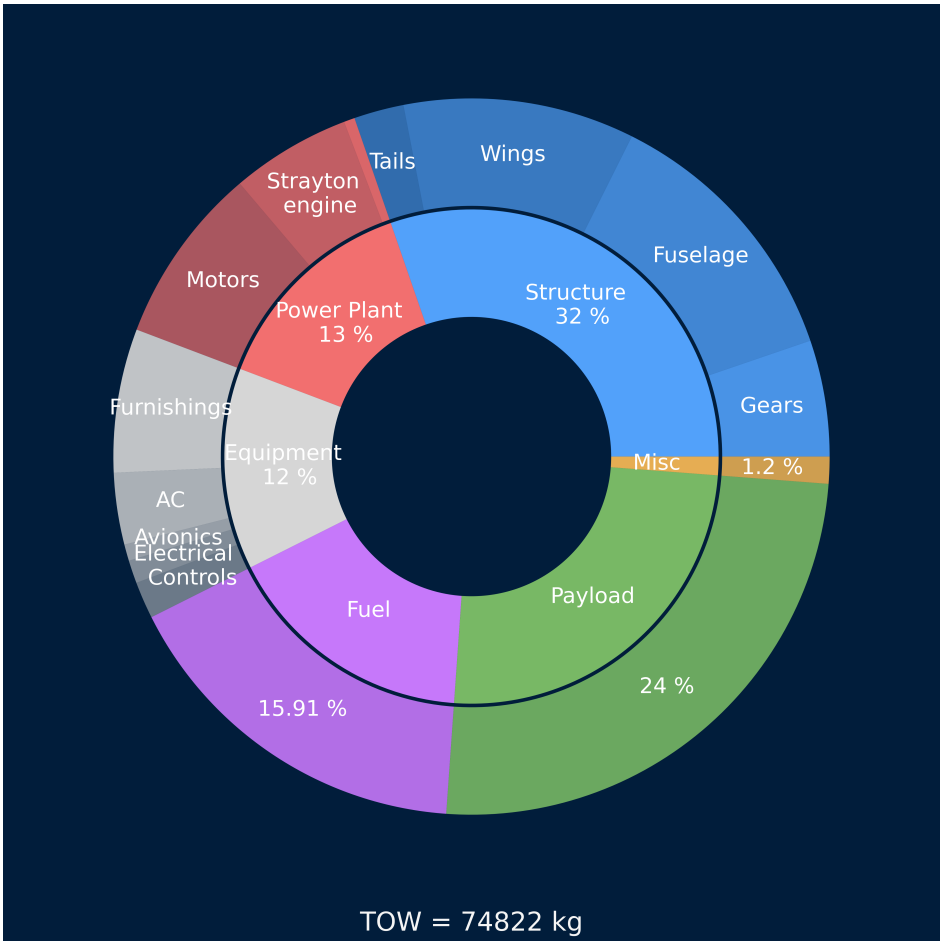


Figure 21: TOW Strayton Kerosene model

6 Conclusions and Future Work

6.1 Conclusions and Recommendations

6.2 Integration with the TREES System

One of the most promising aspects of the Strayton Engine is the natural integration with the TREES system for aircraft thermal management [10]. The TREES system struggled to capture performance gains on traditional turboprop and turbofan powered aircraft due to the inefficiencies and net power loss that result when extracting heat from a post-combustion exhaust. However, the Strayton engine design utilizes acoustic waves as a part of the embedded Stirling cycle, and therefore provides a natural synergy with the TREES technology. Future work is needed to study the performance of a next-gen aircraft thermal managament system build on the foundation of these two technologies.

6.3 Clean Sheet Design Studies

To this point, all work has looked exclusively at retrofits of existing aircraft, but work still remains in studying what designs are optimal when the Strayton engine is selected as the primary power source when doing a clean sheet design.

6.4 Higher Fidelity Models

As a first Strayton engine integration study, this work has relied essentially on low-fidelity models. The assumptions made allowed us to have a first glimpse at what are the prospects of this new technology. However the numbers obtained could vary in future work with higher-fidelity models. In this section we present the major assumptions that could potentially lead to change in the results in a future study.

For both models, as no electrical engine of this scale has been developed yet, we made the assumption that their weight was equivalent to the entire previous jet engine, including the ducted fan. To this first weight, we add the weight of an other ducted fan. This is a very pessimistic assumption considering that normal weight ratio between electric and thermal engine is 1/10.

As presented in Section 4, the present Strayton engine is not considered as low fidelity model since the efficiency depends on various thermodynamic variables. However to even improve its accuracy, the engine could be modeled in PyCycle framework [11], which is a thermodynamic cycle modeling library built on OpenMDAO and compatible with OpenConcept.

The propulsion models for the B737–800 presented in the Section 3 could be improved on several points:

- The efficiency of the electrical motor is a constant. In future work, this model could integrate a 3D engine map where the efficiency would depend on the rotation speed and the torque. To help build such a map, demonstrators are being built and first data could be available in the near future.
- The ducted fans efficiency is considered constant. In future work, these ducted fans could be modeled in PyCycle as compressors and integrate a fan map.

The models used for ATR72–600 propulsion are OpenConcept native library high-fidelity elements. he SimplePropeller element integrates multiple maps and propeller coefficients calculation. It is considered to be a high-fidelity model. However the number of blades is not accurate since this element can model 3 or 4 blade-propellers and this aircraft has 6 blade-propellers. In a future work, we could potentially integrate the propeller map for a 6-blade propeller.

We believe that the combination of the assumptions presented above can have a significant impact on the performance computed in the study. Some of them have a net-negative impact on fuel consumption -weight pessimistic estimation-, whereas others have a net-positive impact -constant efficiency of the electrical motor regardless of the flight segment. It is therefore difficult to predict what could be the performance of higher-fidelity aircraft models, but we can expect a 10% order of magnitude variation for the final numbers.

References

1. Adler, E., and Martins, J. R. R. A., "Hydrogen-Powered Aircraft: Fundamental Concepts, Key Technologies, and Environmental Impacts," *Preprint Submitted to Progress in Aerospace Sciences*, 2023, pp. 1–65. URL `https://www.researchgate.net/publication/366157885_Hydrogen-Powered_Aircraft_Fundamental_Concepts_Key_Technologies_and_Environmental_Impacts`.

2. Dyson, R. W., "True Zero Emission Electric Aircraft Propulsion Transport Technology," *AIAA AVIATION 2023 Forum*, American Institute of Aeronautics and Astronautics, Reston, Virginia, 2023, pp. 1–34. doi:10.2514/6.2023-3987.

3. Brelje, B. J., and Martins, J. R., "Development of a Conceptual Design Model for Aircraft Electric Propulsion with Efficient Gradients," *2018 AIAA/IEEE Electric Aircraft Technologies Symposium*, American Institute of Aeronautics and Astronautics, Reston, Virginia, 2018. doi:10.2514/6.2018-4979.

4. Gray, J. S., Hwang, J. T., Martins, J. R. R. A., Moore, K. T., and Naylor, B. A., "OpenMDAO: an Open-Source Framework for Multidisciplinary Design, Analysis, and Optimization," *Structural and Multidisciplinary Optimization*, Vol. 59, No. 4, 2019, pp. 1075–1104. doi:10.1007/s00158-019-02211-z.

5. McDonald, R. A., and Gloudemans, J. R., "Open vehicle sketch pad: An open source parametric geometry and analysis tool for conceptual aircraft design," *AIAA SciTech 2022 Forum*, 2022, p. 0004.

6. Raymer, D. P., *Aircraft Design: A Conceptual Approach*, American Institute of Aeronautics and Astronautics (AIAA), 2012.

7. O'Hayre, R., Cha, S.-W., Colella, W., and Prinz, F. B., *Fuel Cell Fundamentals*, John Wiley & Sons, Inc, Hoboken, NJ, USA, 2016. doi:10.1002/9781119191766.

8. Bradley, M., "Identification and Descriptions of Fuel Cell Architectures for Aircraft Applications," *2022 IEEE Transportation Electrification Conference & Expo (ITEC)*, IEEE, 2022, pp. 1047–1050. doi:10.1109/ITEC53557.2022.9814063.

9. Lukaczyk, T. W., Wendorff, A. D., Colonno, M., Economon, T. D., Alonso, J. J., Orra, T. H., and Ilario, C., "SUAVE: An Open-Source Environment for Multi-Fidelity Conceptual Vehicle Design," *16th AIAA/ISSMO Multidisciplinary Analysis and Optimization Conference*, American Institute of Aeronautics and Astronautics, Reston, Virginia, 2015, pp. 1–56. doi:10.2514/6.2015-3087.

10. Adler, E. J., Brelje, B. J., and Martins, J. R. R. A., "Thermal Management System Optimization for a Parallel Hybrid Aircraft Considering Mission Fuel Burn," *Aerospace*, Vol. 9, No. 5, 2022, p. 243. doi:10.3390/aerospace9050243.

11. Hendricks, E. S., and Gray, J. S., "pyCycle: A Tool for Efficient Optimization of Gas Turbine Engine Cycles," *Aerospace*, Vol. 6, No. 87, 2019. doi:10.3390/aerospace6080087.